ChemCatChem

Full Papers
doi.org/10.1002/cctc.202001761

Chemistry Europe
European Chemical Societies Publishing

Composition/Performance Evaluation of Lean NO_x Trap Catalysts for Coupling with SCR Technology

Simon Schönebaum,[a, b] Jürgen Dornseiffer,[a, c, d] Peter Mauermann,[a, e] Bernd Wolkenar,[a, e] Stefan Sterlepper,*[a, e] Egbert Wessel,[d, f] Riza Iskandar,[a, g] Joachim Mayer,[a, d, g] Thomas E. Weirich,[a, g] Stefan Pischinger,[a, d, e] Olivier Guillon,[a, c, d, h] and Ulrich Simon[a, b]

The washcoat composition and the catalytic properties of two commercially available lean NO_x traps (LNTs) were investigated. Both catalysts contained nominally the same NO_x storage and catalytic materials but differed strongly in their amount and activity as well as in the composition of their layered washcoat architecture. In lean-rich cycle experiments under realistic engine-out gas compositions using a laboratory gas test bench, the LNTs showed comparable NO_x storage behavior. At temperatures below 250 °C, the lean phase durations last up to 300 s until 50 % of the NO_x storage capacity is reached. The simultaneously calculated NO_x storage efficiencies drop rapidly below 35 %, resulting in a high NO_x slip. Strong variations were observed in N_2O and NH_3 selectivity and in CO slip during regeneration of both LNTs caused by the different oxygen storage capacity (OSC), water gas shift (WGS) activity and rhodium distribution in the catalytic layers. Based on the obtained results, proposals were made to optimize the storage and regeneration performance, leading to highly efficient LNT catalysts for coupling with a downstream SCR catalyst.

Introduction

With the increased awareness towards anthropogenic environmental pollution over the last decades, multiple approaches have been proposed to tackle this issue. A prominent solution is minimizing air pollution arising from road traffic. This refers especially to nitrogen oxides (NO_x), which are mainly emitted by combustion engines. In the exhaust gases of conventional gasoline engines equipped with a three-way catalyst, NO_x can easily be reduced with the present hydrocarbons and carbon monoxide (CO). This is not possible for lean-burn engines due to a lack of reducing compounds in the net oxidizing exhaust gas atmosphere.[1,2] Since lean-burn engines have a higher efficiency compared to gasoline engines operated with a stoichiometric air/fuel ratio, their importance for road traffic has increased in past decades.[3] Due to the continuous tightening of NO_x emission limits,[4,5] it is mandatory to reduce NO_x concentrations in the exhaust gas by in-engine measures and by effective catalytic exhaust gas aftertreatment. As a result, lean NO_x traps (LNTs) and the selective catalytic reduction of NO_x (SCR) are indispensable approaches to effectively remove NO_x from exhaust gases of lean-burn engines.

To achieve NO_x abatement by SCR, a separate reductive is added into the exhaust gas stream. In most cases an aqueous

---

[a] Dr. S. Schönebaum, Dr. J. Dornseiffer, P. Mauermann, B. Wolkenar,
S. Sterlepper, Dr. R. Iskandar, Prof. J. Mayer, Prof. T. E. Weirich,
Prof. S. Pischinger, Prof. O. Guillon, Prof. U. Simon
Center for Automotive Catalytic Systems Aachen (ACA)
RWTH Aachen University
Schinkelstraße 8
52062 Aachen (Germany)
E-mail: Sterlepper@aca.rwth-aachen.de

[b] Dr. S. Schönebaum, Prof. U. Simon
Institute of Inorganic Chemistry (IAC)
RWTH Aachen University
Landoltweg 1
52074 Aachen (Germany)

[c] Dr. J. Dornseiffer, Prof. O. Guillon
Institute of Energy and Climate Research: Materials Synthesis and Processing (IEK-1)
Forschungszentrum Jülich
Leo-Brandt-Straße
52425 Jülich (Germany)

[d] Dr. J. Dornseiffer, Dr. E. Wessel, Prof. J. Mayer, Prof. S. Pischinger,
Prof. O. Guillon
JARA-ENERGY
Wilhelm-Johnen-Straße
52425 Jülich (Germany)

[e] P. Mauermann, B. Wolkenar, S. Sterlepper, Prof. S. Pischinger
Institute for Combustion Engines Aachen (VKA)
RWTH Aachen University
Forckenbeckstraße 4
52074 Aachen (Germany)

[f] Dr. E. Wessel
Institute of Energy and Climate Research: Microstructure and Properties (IEK-2)
Forschungszentrum Jülich
Leo-Brandt-Straße
52425 Jülich (Germany)

[g] Dr. R. Iskandar, Prof. J. Mayer, Prof. T. E. Weirich
Central Facility for Electron Microscopy (GFE)
RWTH Aachen University
Ahornstraße 55
52074 Aachen (Germany)

[h] Prof. O. Guillon
Institute of Mineral Engineering (GHI)
RWTH Aachen University
Mauerstraße 5
52064 Aachen (Germany)

urea solution – known as AdBlue® or diesel exhaust fluid (DEF) – is used as precursor of NH_3.[6,7] After injection into the exhaust gas stream, the urea decomposes in two steps via isocyanic acid (HNCO) to form NH_3 and CO_2. At low temperatures, the deposition of byproducts on the injector, the piping and on the catalyst surface resulting from the incomplete hydrolysis of HNCO still poses significant challenges for commercial applications.[8] The generated NH_3 is subsequently adsorbed on the SCR catalyst surface and used for the continuous selective reduction of NO_x to N_2 and H_2O.

In contrast to the SCR reaction pathway, exhaust gas aftertreatment via LNTs is executed in two alternating working states. First, in the standard operation condition (lean phase) of the engine, NO_x from the raw, oxygen-rich emissions is stored in the catalyst.[9,10,11] After a period of 60–120 s,[12,13,14] depending on the raw emission composition and the driving profile, the storage is filled and needs regeneration. This is achieved by fuel-rich combustion with excessive H_2, CO and hydrocarbons in an O_2-deficient exhaust gas atmosphere. After a reduction period of normally 3–10 s, the catalyst is regenerated and the engine switched back to lean-burn operation.[12,13,15]

In the 1990s, Toyota[16] developed an LNT containing Pt-BaO/Al_2O_3. Here, the NO_x – mainly composed of NO[17] – is oxidized to NO_2 by Pt during the lean phase and afterwards chemisorbed as nitrites or nitrates[9] by neighboring BaO particles. In the rich phase, well-dispersed Pt nanoparticles serve for the reduction of the desorbed NO_x, which is mainly reduced to N_2; side products such as N_2O and NH_3 may be formed.[18,19,20] However, this catalyst material lacks low-temperature activity ($<250\,°C$)[21] as well as suitable stability with respect to sulfur.[22] To overcome these limitations, several new materials with additional functionalities have been integrated in the washcoat of modern commercially used LNTs.

Alkaline or alkaline-earth metal oxides (e.g. Ba, K, Sr) with strong Lewis basic properties still serve for the chemisorptions of NO_x.[23] Within the washcoat these are either supported on oxides such as alumina or present as pure particles. In both cases, Pt is dispersed on this active phase. To improve SO_2 tolerance, Pd is also used here, but at the expense of NO oxidation activity.[24,25] To enhance the low-temperature activity of the catalyst, Pt/CeO_2 is added as another main component. CeO_2 itself is an active NO_x storage material, whose storage and oxidation activity starts at temperatures as low as 25–50 °C.[26,27] Additionally, at 200 °C it is capable of storing nitrites as well as nitrates in an NO-containing atmosphere, which means it is able to oxidize NO without the presence of precious metals.[28] Furthermore, Pt/CeO_2 also improves the regeneration of the LNT during the rich phase. On one hand, the nitrates formed are more easily desorbed from ceria compared to BaO.[29] On the other hand, Pt/CeO_2 strongly catalyzes the water gas shift reaction (WGS).[30,31] CO as a harmful exhaust gas component is therefore removed and H_2 is generated. The latter serves as a highly efficient reductive of NO_x especially at low temperatures.[32] In some cases, Pt/CeO_2 can be found as a coating on Al_2O_3, which also enhances the storage activity as well as the aging stability.[33] Nevertheless, pure stabilized ceria grains are also sometimes used as a support for Pt/BaO to improve its LNT performance.[34] To further enhance the low-temperature NO_x adsorption of LNTs, mixed Al/Mg oxides or spinels can be added as support material for Pt. These materials are derived from hydrotalcites by calcination and offer higher low-temperature storage activity ($<200\,°C$). Moreover, such materials also provide better resistance to SO_2 compared to $Pt/BaO/Al_2O_3$ systems[35,36] and can be further improved by adding Cu as an active compound.[37]

To strengthen the reduction properties during the rich phase, current LNTs also contain Rh as an active component. Depending on the support, Rh has different catalytic properties: Rh/ZrO_2 is known to effectively catalyze the steam reforming[38] of hydrocarbons into H_2, which is provided for the NO_x reduction, whereas Pt–Rh/CeO_2 strongly promotes H_2 generation via the WGS reaction.[39] Rh is usually not applied on the Al_2O_3 support since Rh_2O_3 has an isomorphic structure and a diffusion of Rh into the alumina lattice leads to the deactivation of the precious metal. However, the generation of H_2 on supports other than Al_2O_3 not only improves the regeneration performance, but also the resistance to poisoning by SO_2.[40] In some cases, zeolites mostly platinized are also included in LNT catalysts although they do not offer NO_x storage capability. Their main task is to prevent hydrocarbon slip during the cold start phase of the engine arising from too low oxidation activity of the catalyst below 200 °C. The unreacted hydrocarbons are buffered in the zeolite pore structure until the catalyst reaches the light-off temperature and thus oxidation activity is reached.[41]

To address the current restrictive legislation for real driving emissions, a combination of LNT and SCR catalysts is a possible pathway[42] to increase the NO_x abatement efficiency. This is already commercialized in some serial production vehicles (Volvo, Audi). Different concepts are applied: Coupling LNT with a passive SCR downstream catalysts[14,43,44,45,46] uses the NH_3 emitted during the regeneration of the LNT, leading to an improvement in the NO_x reduction between 5 and 12% at similar CO_2 emissions compared to the baseline variant. A close to stoichiometric ratio of NH_3/NO_x downstream of the LNT can be achieved by optimizing the rich purge concentrations and duration between 250 and 350 °C, but at the cost of increasing N_2O production.[13] The implementation of longer lean times leads to significant improvements in the trade-off between additional CO_2 production (fuel consumption in rich purge) and NO_x emissions[45] along with a NO_x conversion above 90% at 250 °C.[44] Here, the SCR catalyst converts the slipping NO_x, while at the same time more NH_3 is produced in the rich purges. For coupling with an active SCR, a reduction in AdBlue® consumption by up to 55% with a low increase in fuel consumption at the same tailpipe NO_x level can be achieved.[46] A suitable LNT for this application has to fulfill several requirements: Fast NO oxidation to storable NO_2 and a high storage capacity at low temperatures in an extended lean phase as well as effective NO_x reduction in the rich phase with high selectivity towards ammonia. These requirements have to be met without impacting the long-term stability with respect to temperature as well as sulfurization of current LNT catalysts.[47,48,49,50,51,52,53,54]

Table 1. Element composition of the LNT catalysts determined by ICP-OES. All values are given in gram per liter catalyst volume with generic error accounts below 2 %.

Catalyst	Pt	Pd	Rh	Ce	Ba	Mg	Zr	Nd	La
LNT 1	3.36	0.70	0.15	130	28.45	n.a.	15.75	1.74	–
LNT 2	2.52	0.77	0.09	108	8.93	3.79	0.19	–	1.77

n.a.: not analyzed

Publications concerning the performance of fully formulated LNT systems mainly deal with operating strategies,[55] aging and poisoning effects,[56,57,58,59] the influence of cycling conditions on NO_x conversion and selectivity of product gas components[60,61] as well as kinetic modeling[62] for single LNT operation. However, these studies do not examine the required LNT performance for coupling with SCR catalysts. In this application it is crucial to utilize individual control strategy to trigger the LNT regeneration according to the SCR activity. As a result, long lean phases up to 900 s could be achieved before draining the LNT from its high NO_x loading level in a short rich event.

In the present paper, we examine the washcoat composition as well as the storage behavior and the regeneration performance of LNT catalysts for such long lean phases. In addition, we demonstrate how a detailed analysis can help to design tailor-made washcoat compositions to further optimize LNT for use within coupled LNT-SCR systems. In this regard, two different, commercially available LNTs were investigated with respect to their phase and washcoat configuration by means of x-ray powder diffraction (XRD), inductively coupled plasma optical emission spectrometry (ICP-OES), scanning electron microscopy (SEM) and transmission electron microscopy (TEM). Additionally, the latter two were combined with element mappings by energy-dispersive x-ray spectroscopy (EDX). Different washcoat components were therefore identified and assigned to their tasks within the LNT. Furthermore, the storage and regeneration behaviors of the LNTs were investigated by extensive laboratory gas test bench (LGB) studies under realistic engine-out exhaust gas compositions and air/fuel ratio (lambda) situations. In lean-rich cycle experiments, the storage capacities were evaluated in the temperature range of 150 to 450 °C and the regeneration efficiencies at three different durations between 5 and 20 s were calculated including the selectivity for the emitted nitrogen-containing species. For this purpose, the lean phase duration was extended up to 900 s to ensure comparable NO_x loading situations at every adjusted temperature and to compare the time-dependent adsorption with respect to the filling level and the regeneration behavior. To complete the catalyst benchmark, we evaluated the oxygen storage capacities (OSC) as a crucial parameter for the selectivity towards ammonia and nitrous oxide. In a subsequent assessment of the catalytic properties, we demonstrate the drawbacks of commercial LNTs and suggest pathways to overcome these in future LNT-SCR or LNT-SDPF applications.

Results and Discussion

Catalyst characterization

Element composition

For catalyst characterization, the main element compositions of the catalysts were first determined by ICP-OES and summarized in Table 1. Pt, Pd and Rh were found in both LNTs with a total specific PGM loading of 4.21 g/l (LNT 1) and 3.38 g/l (LNT 2), respectively. Apart from a comparable amount of ceria, LNT 1 had a much higher Ba content compared to LNT 2. Additionally, a specific amount of 3.79 g/l of Mg was found in LNT 2. The concentration of Mg in the washcoat of LNT 1 could not be estimated due to a high Mg concentration in the cordierite monolith. Moreover, Nd was detected in LNT 1 and a comparable amount of La was found in LNT 2. These elements are typically used for thermal stabilization of the contained oxides and are not further discussed here.[63,64]

Phase composition

XRD analyses of the peeled washcoats were performed to determine the different phase compositions present. The results (Figure 1) reveal that both LNTs contain crystalline phases of CeO_2 and $BaCO_3$ as well as $MgAl_2O_4$. Concerning the reflection intensities and peak widths for $MgAl_2O_4$, broader reflection peaks were observed in LNT 2, indicating smaller particle sizes

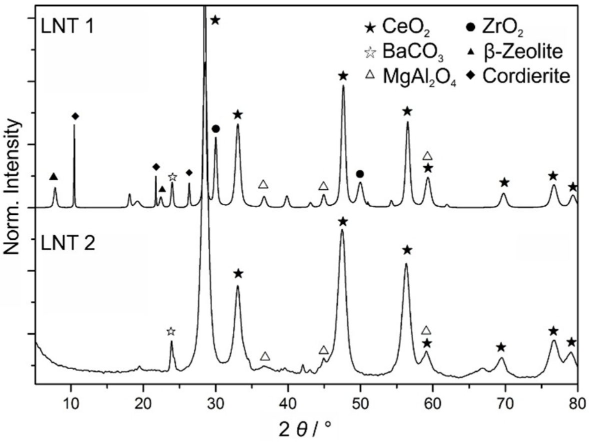

Figure 1. XRD pattern of the LNT 1 and LNT 2 washcoat. Reflections are assigned to the corresponding crystalline structures (symbols).

compared to LNT 1. Additionally, the washcoat of LNT 1 includes β-zeolite, ZrO_2 and Cordierite which appears as an impurity in the sample after scratching the washcoat off the ceramic monolith. No crystalline alumina phase was found in either sample. Insignificant amounts of other crystalline structures were detected but not further evaluated.

SEM investigations

SEM investigations of the catalysts were performed for a basic characterization of the washcoat architectures (Figure 2). LNT 1 is based on a ceramic monolith, LNT 2 on a metallic foil monolith. Both have a comparable cell density of 400 cpsi but differ in the washcoat appearances (Table 2).

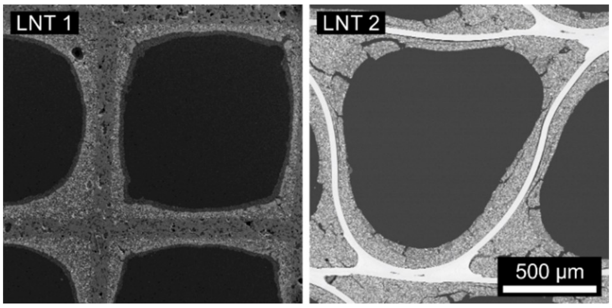

Figure 2. Cross-section SEM images from the LNT catalysts; LNT 1 with a ceramic monolith, LNT 2 with a metallic foil monolith.

The element mappings of LNT 1 (Figure 3) revealed that the ceramic honeycomb structure consists of mixed Si/Mg/Al oxide, identified as cordierite by XRD. The washcoat was formed from three separate layers. In the bottom layer (1) with an approximate thickness of 50–80 µm, two different major components were distinguished: Besides a mixed $MgAl_2O_4$ spinel phase, nearly pure ceria (both confirmed by XRD) was identified. Ba was found to be evenly distributed over all the particles of the base layer. The relatively thin middle layer (2) had a thickness of only about 2–15 µm. EDX analyses revealed the presence of both, zirconia and alumina. Here, alumina was used as a binder for the ZrO_2 phase. Ba was also present in this layer, but in higher concentration compared to the bottom layer. The top layer (3), facing towards the channel center, consisted of mainly Si and some Al. Within this layer, alumina was also used as a binder, but for β-zeolite.

The element mappings of LNT 2 reveals that the washcoat is comprised of only two distinct layers (Figure 4). In the bottom layer (1) with a thickness of approx. 80 µm, four different compounds were identified: Besides $MgAl_2O_4$, a pure alumina phase was present, which was not detected by XRD. Additionally, separate Ce- and Ba-containing particles were identified, which were found by XRD in the form of CeO_2 or $BaCO_3$, respectively. The top layer (2) with a thickness of approx. 60 µm was found to include two different kinds of particles: A CeO_2 phase as well as pure alumina particles, however, the Ce concentration was lower in the top layer compared to the base layer.

Table 2. Honeycomb and washcoat characteristics of the LNT catalysts determined by SEM.

Catalyst	Honeycomb material	Cell density [cpsi]	Wall thickness [µm]	Washcoat thickness [µm] channel sides	corners
LNT 1	Cordierite	400	127	106 ± 29	194 ± 59
LNT 2	Metal foil	400	50	80 ± 27	230 ± 148

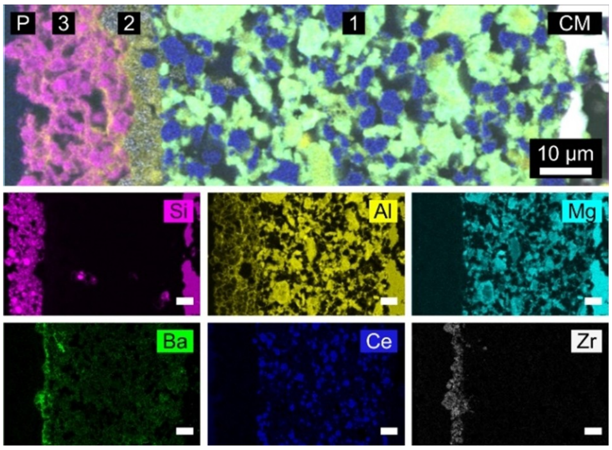

Figure 3. Cross-section SEM image (top) and element mappings (below) of the washcoat of LNT 1. 1: Bottom layer, 2: Middle layer, 3: Top layer. The right border of all images points towards the ceramic monolith (CM). Scale bars in all images represent 10 µm.

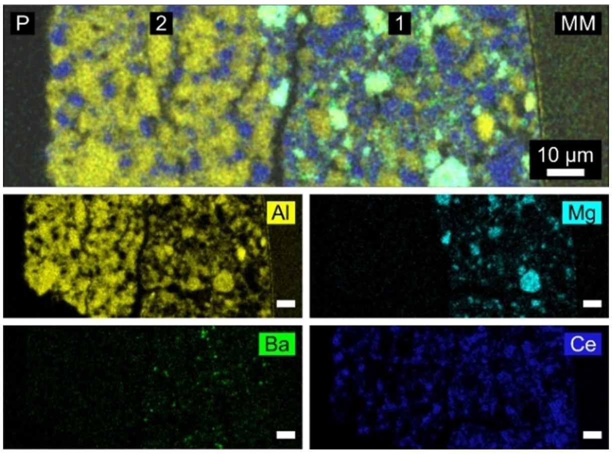

Figure 4. Cross-section SEM image (top) and element mappings (below) of the washcoat of LNT 2. 1: Bottom layer, 2: Top layer. The right border of all images points towards the metal foil monolith (MM). Scale bars in all images represent 10 µm.

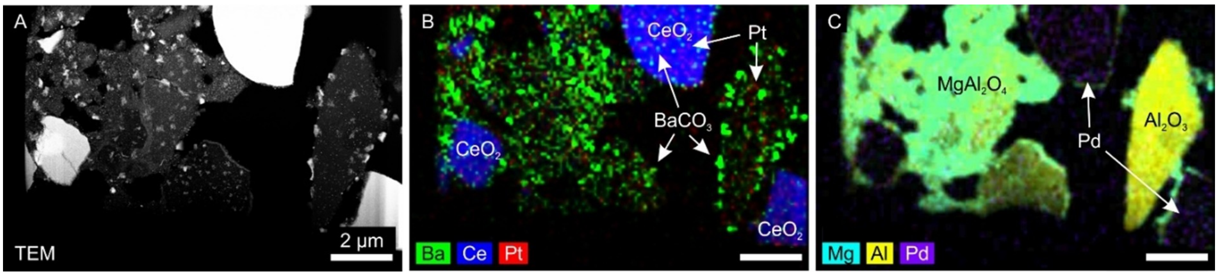

Figure 5. HAADF-TEM image (A) of a FIB lamella taken from the bottom layer of LNT 1 and combined EDX element mappings of the whole lamella (B, C). Scale bars in all images represent 2 µm.

TEM investigations

To obtain detailed local information about PGM loadings and the element distribution within the washcoat components, focused ion beam (FIB) lamellae were prepared from each layer of the catalysts and analyzed by TEM.

In the bottom layer of LNT 1, in addition to $MgAl_2O_4$ and ceria, a pure alumina phase was found (Figure 5). Small $BaCO_3$ particles were identified all over the alumina and spinel phases as well as on the ceria phase. Regarding precious metals, Pt and Pd phases were found to be distributed all over the alumina, ceria and spinel phases.

Comparable investigations on a lamella of the middle layer (Figure 6, B) showed that the ZrO_2 grains were loaded with highly dispersed Rh nanoparticles. However, the signal for Rh was close to the detection limit and no Rh nanoparticles were observed during the investigation. Here, the existence of the ZrO_2 phase is an additional indication of the presence of Rh (which was also detected by ICP-OES), since it is usually applied as Rh support instead of Al_2O_3. The zeolite particles of the top layer (Figure 6, A) were bound with pure alumina and loaded with large single Pt particles in the size range of up to 62 nm.

In the case of LNT 2, four oxide phases were identified in the bottom layer (Figure 7). In addition to alumina and spinel particles, separate $BaCO_3$ and ceria phases were also present. However, in comparison to LNT 1, no BaO coating was spotted on the ceria. Further analysis showed that Pt was distributed in the form of well-dispersed nanoparticles over the pure alumina, ceria and the $MgAl_2O_4$ phase in the bottom layer, whereby the detected concentration on the alumina particles was much higher. Only minor amounts of Pt were detected on the ceria phase. In the top layer (Figure 8), only ceria and a binding alumina phase were found. The latter was loaded with Rh, Pd and Pt. As part of the TEM investigation, an agglomerate of Rh with a particle size of approx. 300 nm and a neighboring Pt

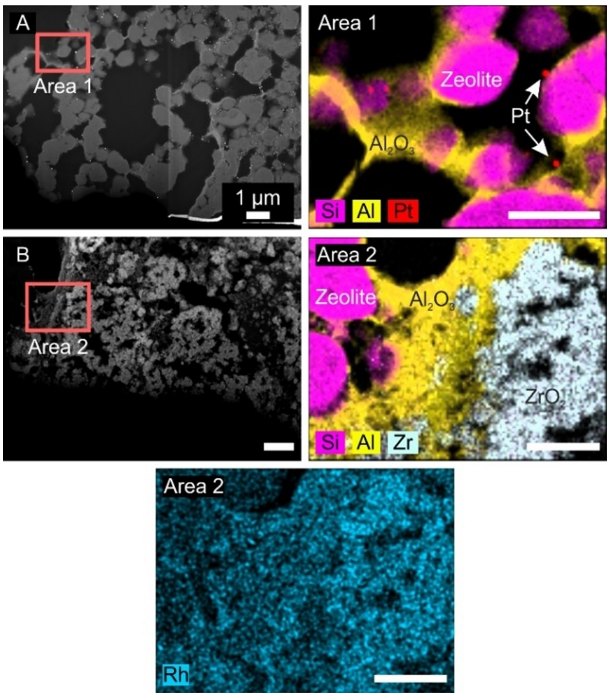

Figure 6. HAADF-TEM images of a FIB lamellae taken from the from top (A) and middle (B) layer of LNT 1 and combined EDX element mappings of the selected areas (Area 1, Area 2). All scale bars represent 1 µm.

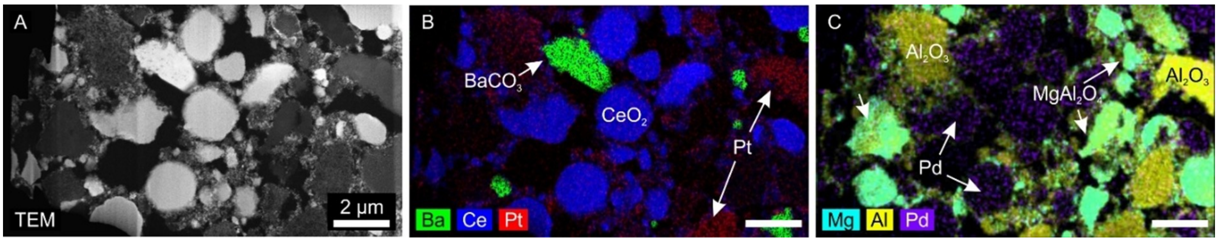

Figure 7. HAADF-TEM image (A) of a FIB lamella taken from the bottom layer of LNT 2 and combined EDX element mappings of the whole lamella (B, C). Scale bars in all images represent 2 µm.

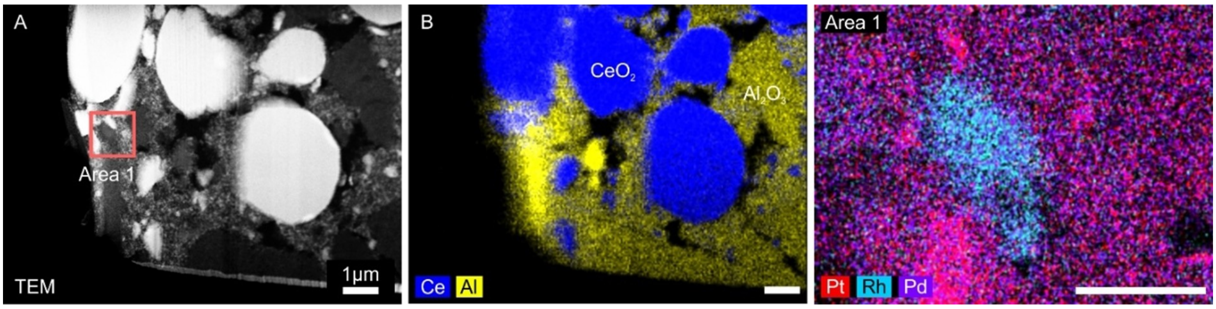

Figure 8. HAADF-TEM image (A) of a FIB lamella taken from the top layer of LNT 2 and combined EDX element mappings of the whole lamella (B) and selected areas (Area 1). Scale bars in all images represent 1 µm.

particle was also located on the alumina phase next to the well-dispersed Pt/Pd (Figure 8, Area 1).

The obtained analysis results of both LNTs concerning their layer compositions and precious metal loadings are summarized in Table 3. In LNT 2 the main NO_x storage compounds are located in the bottom layer, whereas the composition of the top layer is designed to enhance the regeneration behavior in the rich phase. Besides the Rh loaded alumina, which has a high selectivity towards N_2 during NO_x reduction, Pt on ceria was also found in this layer. As a highly active low temperature WGS catalyst this composite increases the H_2 concentration in the regeneration gas, which is the most efficient reductive for NO_x. Additionally, a Pd coating was found on the alumina in the top layer. This precious metal normally does not support the regeneration, but is a high active catalyst to oxidize hydrocarbons and CO during lean operation. This strict separation was not observed in LNT 1. Here, only the Rh loaded on the zirconia was found in a separate layer below the zeolite containing top layer, which enhances the cold start performance of the LNT. All other phases and functionalities are located in a separate bottom layer.

Table 3. Layer compositions of the compared LNTs obtained by XRD, SEM-EDX and TEM-EDX

Component	LNT 1	LNT 2
Bottom layer	CeO_2 loaded with $BaCO_3$, Pt, Pd $MgAl_2O_4$ loaded with $BaCO_3$, Pt, Pd Al_2O_3 loaded with $BaCO_3$, Pt, Pd	CeO_2 loaded with minor amounts of Pt $MgAl_2O_4$ loaded with Pt Al_2O_3, loaded with high amounts of Pt $BaCO_3$
Middle layer	ZrO_2 loaded with Rh	-
Top layer	Zeolite β loaded with Pt Alumina binder phase	CeO_2 loaded with minor amounts of Pt Al_2O_3 loaded with Rh, Pd, Pt

Catalytic performance

NO_x storage behavior

One of the main characteristic properties of LNTs is their NO_x storage capacity (NSC) and regeneration behavior, since only the stored NO_x species can be converted to N_2, or to NH_3 in the following rich phase for further use in a downstream SCR catalyst. To assess the NO_x storage behavior of both LNTs, lean-rich cycling experiments were performed after hydrothermal aging at 750 °C following the procedure described in the Experimental section. For this evaluation, the dosed NO is labeled as $NO_{x,dos}$, since NO_2 was dosed. The sum of slipped NO as well as NO_2 is indicated as $NO_{x,slip}$.

A representative presentation of a typical lean-rich cycling experiment is given in Figure 9. Here, the storage behavior of LNT 1 at 250 °C with a rich phase duration of 10 s is evaluated. During the rich phases, high concentrations of desorbed NO_x ($NO_{x,slip}$, red curve) were observed. The cycle-related NO_x storage $NO_{x,st}$, (blue curve) was calculated as the cumulative value of the difference between c($NO_{x,dos}$) and c($NO_{x,slip}$) during the lean phases and was set to zero after each lean phase. Especially for low temperatures and short regeneration times, a strong

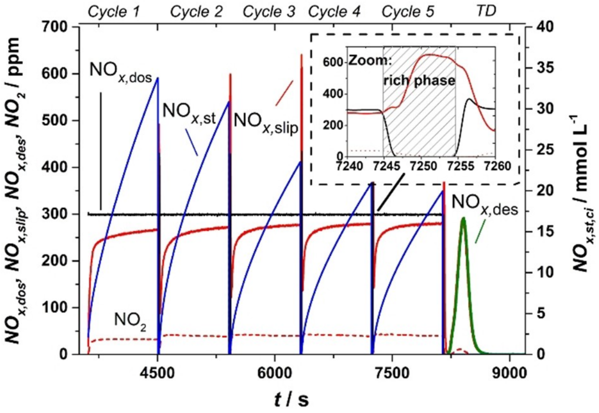

Figure 9. Cumulative, cycle-related NO_x storage behavior ($NO_{x,st}$ blue curve) and NO_x slip ($NO_{x,slip}$, red curve) of LNT 1 during five cycles at 250 °C with a regeneration time of 10 s and the NO_x remaining in the catalyst measured after thermal desorption (TD) at 500 °C ($NO_{x,des}$, green curve).

decrease of the cumulative NO_x storage was measured. NO_x storage reached an equilibrium state after at least four lean-rich cycles. After completion of the fifth lean-rich cycle, thermal desorption was performed at 500 °C to estimate the total amount of $NO_{x,des}$ (green curve) and the amount of NO_x remaining on the catalyst after the final regeneration.

First, the storage performance of the LNTs at four different temperatures with regeneration times of 5, 10 and 20 s was evaluated. All used conditions are shown in detail in the Experimental section in Table 4. In nearly all measurements the stored amount of NO_x decreased from cycle to cycle. After four lean-rich cycles, a stable NO_x storage amount was reached. The decrease is caused by incomplete regeneration during the rich phases due to low NO_x desorption speed, a lack of regeneration activity and other insufficiencies. As catalyst pretreatment (thermal desorption up to 500 °C) resulted in a completely depleted LNT in terms of NO_x, the calculated storage capacity from the first lean phase is the maximum possible storage capacity at the corresponding temperature, duration and NO_x concentration. After four lean-rich cycles, a stable NO_x storage capacity was reached. To compare the initial and equilibrium NO_x storage capacities of both LNTs under different conditions, these properties were quantified by first estimating the dosed and slipped amounts of NO_x. The total amount of dosed and slipped NO_x in each cycle i, i.e. between the starting time $t_{sc,i}$ and finishing time $t_{ec,i}$ of NO_x loading, were estimated by Equations (1) and (2), respectively.

$$NO_{x,\mathrm{dos},ci} = \int_{t_{\mathrm{sc},i}}^{t_{\mathrm{ec},i}} c_{NO_{x,\mathrm{dos},ci}} \mathrm{d}t \quad (1)$$

$$NO_{x,\mathrm{slip},ci} = \int_{t_{\mathrm{sc},i}}^{t_{\mathrm{ec},i}} c_{NO_{x,\mathrm{slip},ci}} \mathrm{d}t \quad (2)$$

All values of $NO_{x,st,ci}$ were calculated for each lean phase using the same method, but with the corresponding $t_{sc,i}$ and $t_{ec,i}$ with i = [1..5] using Equation (3).

$$NO_{x,\mathrm{st},ci} = NO_{x,\mathrm{dos},ci} - NO_{x,\mathrm{slip},ci} \quad (3)$$

At the beginning, the general NO_x storage capacity of each LNT at a certain temperature was defined as the amount of stored NO_x during the first lean phase, according to Equation (4).

$$NO_{x,\mathrm{storage\ capacity}} = NO_{x,\mathrm{st,c1}} \quad (4)$$

The resulting changes of the NO_x storage capacities depending on the temperature are shown in Figure 10 for both LNTs.

Generally, both LNTs showed a comparable NO_x storage capacity within the error limits of the experiments performed with the highest NSC in a medium temperature range of 250 to 350 °C. However, LNT 1 reached the highest $NO_{x,st,c1}$ at 310 °C with around 42 ± 2 mmol/l, while LNT 2 revealed a slightly higher value although its maximum was found at 290 °C.

At high temperatures, storage is expected to be limited for both catalysts by the storage capacity of NO_x at the Ba species.[34,65] Here, LNT 1 displays a slightly higher NO_x capacity at 350 °C and more than 40 % at 450 °C compare to LNT 2, although the Ba content of LNT 1 is four times higher than LNT 2. A valid cause for this observation could be the different BaO distribution in the two catalysts. Compared to LNT 2, where the Ba is located in isolated grains within the washcoat, the alkaline earth metal in LNT 1 is distributed as a coating of small particles on and in the alumina as well as on $MgAl_2O_4$ and ceria phases.

At lower temperatures, the storage capacity is influenced by the ceria and $MgAl_2O_4$ phases. In this temperature range, LNT 2 has a higher NO_x storage capacity compared to LNT 1, while LNT 1 has a higher Ce content of 20 % compared to LNT 2. One reason for this finding could be the ceria phase in LNT 1, which was coated with $BaCO_3$. This composite was probably implemented in the bottom layer to improve NO_x storage behavior. Shi et al. reported that $Pt/BaO/CeO_2$ exhibited higher NO_x storage capacity between 200 °C and 300 °C relative to $Pt/BaO/Al_2O_3$ and $Pt/CeO_2/Al_2O_3$ with a superior NO_x storage-reduction performance under cycling conditions in the same temperature range.[34] Our results do not support these findings. Lower loadings of ceria and $BaCO_3$ in isolated phases have a

Table 4. Conditions used for NO_x storage-regeneration cycling experiments at GHSV = 60000 h^{-1}, gases were balanced with N_2

Parameter	Lean (λ = 1.526)	Rich (λ = 0.963)
Duration [s]	360/900/780/300	5, 10, and 20
Temperature [°C]	150/250/350/450	150/250/350/450
NO [ppm]	300	0
C_3H_6 [ppm]	100	1200
H_2 [ppm]	0	4000
CO [ppm]	500	12000
CO_2 [%]	10	10
H_2O [%]	10	10
O_2 [%]	8	0.6

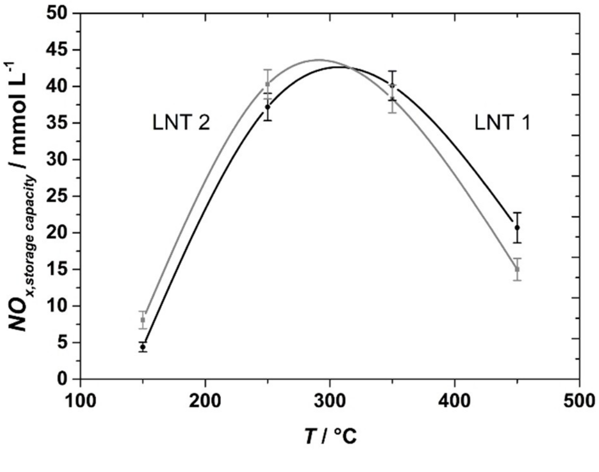

Figure 10. Temperature-dependent NO_x storage capacity of LNT 1 (black line) and LNT 2 (grey line).

comparable storage behavior. A detailed comparison of the dynamic NO_x storage behavior of both LNTs at different temperatures and rich phase durations was performed by evaluating the cycle-related NO_x storage capacity $NO_{x,st,ci}$ for each cycle (Figure 11).

The loss of cycle-specific NO_x storage appeared to be strongly dependent on the regeneration time due to the high NO_x loading level at each evaluated temperature. For all measurements with a rich phase time of 5 s, the decrease of $NO_{x,st,ci}$ to later cycles is visible, resulting in a minimum $NO_{x,st,c5}$ of approx. 2–20 mmol/l for 150 °C, 250 °C and 350 °C, respectively. With an increased regeneration time of 10 s, the storage capacity at 150 °C and 450 °C was nearly stable over five cycles, indicating a full removal of the stored NO_x after each cycle. At 250–350 °C, a less distinct reduction of NO_x storage capacity from 35–45 mmol/l to 20–35 mmol/l was observed. With a maximum regeneration duration of 20 s, a decrease of the specific NO_x storage was only observed at 250 °C. However, starting from 35 mmol/l and 45 mmol/l for LNT 1 and LNT 2, respectively, the specific NO_x storage unexpectedly increased in the second lean cycle to 40 mmol/l and 50 mmol/l followed by a decrease to 30 mmol/l and 45 mmol/l. In general, it was found that in spite of the different washcoat compositions and structures, the NO_x storage behavior of both LNTs is comparable under most conditions.

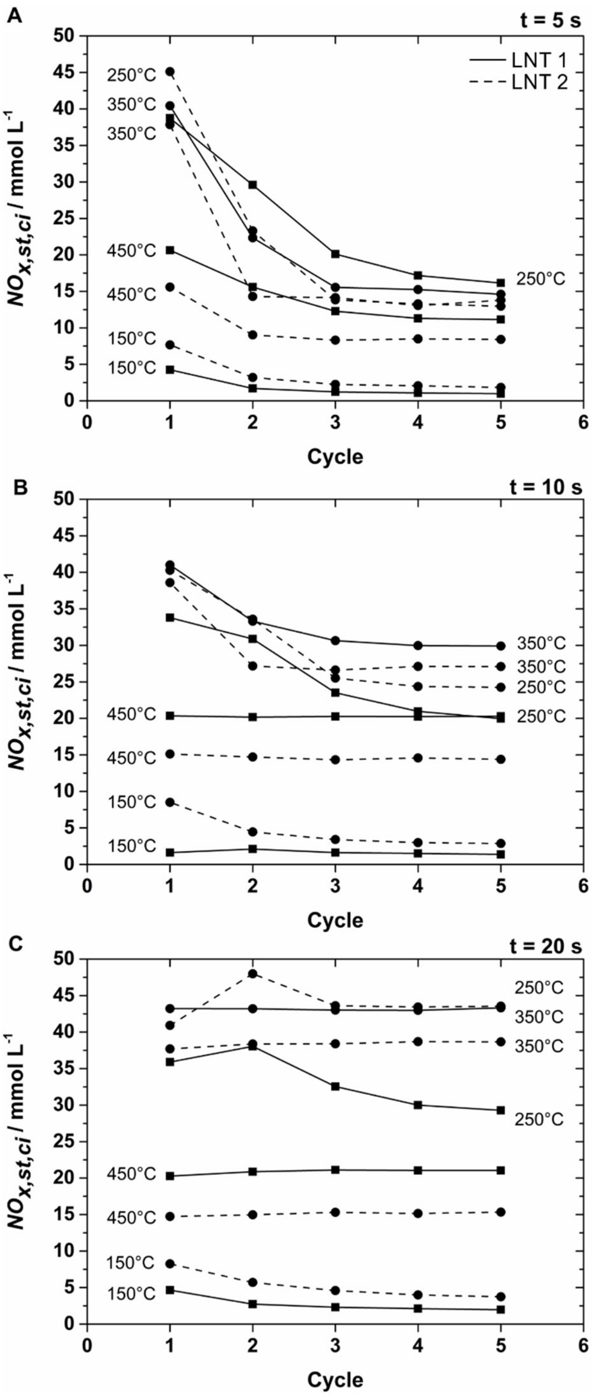

Figure 11. Evolution of the NO_x storage of LNT 1 (solid line) and LNT 2 (dotted line) during five consecutive cycles at different temperatures and rich phase durations of 5 s (A), 10 s (B) and 20 s (C), respectively.

NO_x *storage efficiency*

To evaluate the storage behavior in shorter and more suitable lean phase durations for coupling with a downstream SCR catalyst, we calculated the time-dependent NO_x storage efficiency $\eta_{st,c1}(t)$ during cycle 1 of both LNTs at 250 °C and 350 °C, respectively (Figure 12). The amounts of the NO_x stored $NO_{x,st,c1}(t)$ and of the NO_x dosed during the lean phase $NO_{x,dos,c1}(t)$ were subsequently estimated by Equation (5) and (6), respectively. Finally, $\eta_{st,c1}(t)$ was calculated according to Equation (7).

$$\mathrm{NO}_{x,\mathrm{st,c1}}(t)=\sum_{0}^{t}\mathrm{NO}_{x,\mathrm{st,c1}}(t) \qquad (5)$$

$$\mathrm{NO}_{x,\mathrm{dos,c1}}(t)=\sum_{0}^{t}\mathrm{NO}_{x,\mathrm{dos,c1}}(t) \qquad (6)$$

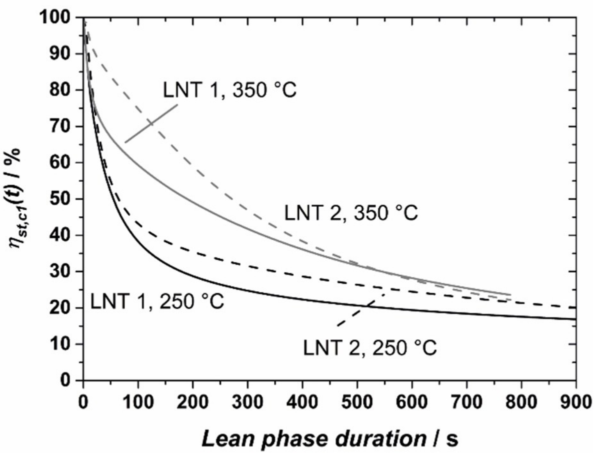

Figure 12. Evolution of time-dependent NO_x storage efficiency $\eta_{st,c1}(t)$ during the first lean phase of LNT 1 (solid line) and LNT 2 (dotted line) at 250 °C (black) and 350 °C (grey), respectively.

$$\eta_{\mathrm{st,c1}}(t)=\frac{\mathrm{NO}_{x,\mathrm{st,c1}}(t)}{\mathrm{NO}_{x,\mathrm{dos,c1}}(t)}\cdot 100\,\% \tag{7}$$

In the first few seconds of the lean phase at 250 °C, the dosed NO_x was nearly completely adsorbed on the catalysts resulting in a high NO_x storage efficiency of more than 98 %. With time, the $NO_{x\ \mathrm{slip}}$ increases dramatically leading to a corresponding decrease of $\eta_{\mathrm{st,c1}}(t)$ down to 20 % after 900 s with a total NO_x loading of 38 mmol/l, whereas 50 % of the storage was filled after 300 s. In principle, this behavior was observed at all investigated temperatures, but its shape changed due to the washcoat composition at temperatures above 350 °C.

Nevertheless, these findings cannot be directly applied to determine an efficient NO_x abatement strategy for an engine at real operating conditions with a downstream coupled SCR catalyst, since the time-dependent storage efficiency is strongly influenced by the NO_x concentration in the gas phase and by the type of exposure, e.g. NO_x peaks. Due to this complex coherence, only an estimation of a suitable operation range of combined LNT-SCR systems can be calculated with these performance determinations under steady state conditions. On the one hand, shorter NO_x loading phases increase the storage efficiency, but at the same time they reduce the duration of the lean phase. Consequently, the regeneration frequency increases resulting in higher specific fuel consumption and additional CO_2 emissions. On the other hand, longer lean phases result in a higher NO_x slip, which has to be converted downstream in the SCR catalyst for high overall NO_x abatement. Since for the investigated LNTs an effective storage can be reached only within 200 s at each evaluated temperature, the operating range of a LNT to optimize the interplay with an SCR catalyst is quite small. One possibility to overcome these limitations is the development of new NO_x storage materials with improved storage capability, especially at temperatures around and below 200 °C.

NO_x slip during regeneration

In all lean-rich cycling experiments, high NO_x slips during the rich phases were observed (see Figure 9), irrespective of the investigated LNT. This behavior was caused by a temperature increase inside the catalysts during regeneration resulting mainly from the exothermal oxidation of the reducing agents (H_2, CO) with residual O_2 (6000 ppm dosed) in the realistic rich phase gas composition representing a lambda situation of $\lambda=0.963$. Figure 13 illustrates the temperature evaluation inside of both LNTs and the corresponding NO_x slip during a 20 s regeneration at 250 °C. This temperature peak leads to a sudden NO_x desorption that cannot be directly reduced by the residual H_2 and CO in the washcoat. This has to be considered while evaluating the amount of reduced NO_x during the rich phase.

For LNT 1 with a temperature increase up to 340 °C, the observed NO_x slip was only 500 ppm for a few seconds. In contrast, LNT 2 revealed a more intense rise in catalyst temperature to 365 °C probably caused by the lower heat capacity of the metallic monolithic support and by different OSC results in a strong NO_x desorption with a maximum concentration of 1000 ppm for a longer period. This small temperature difference of about 25 °C could not only be the reason for the significant higher NO_x release during regeneration of LNT 2. While LNT 1 has a higher storage capacity at 350 °C, the primary desorbed NO_x during a rich phase can be more effectively buffered in this washcoat.

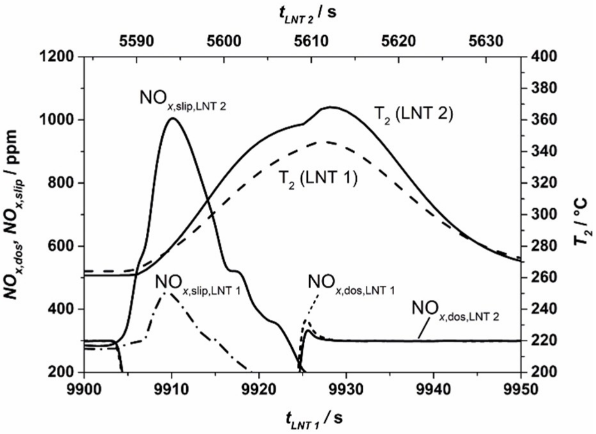

Figure 13. Comparison of the temperature evaluation (T2) inside LNT 1 (dotted line) and LNT 2 (solid line), and NO_x slip during regeneration of 20 s at 250 °C. Position of the thermocouple T2 in the catalyst samples see Figure 22 B.

The increased temperature during the rich phase also affects the catalyst temperature during the first 30 s of the following lean phase. Since for both LNTs the maximum NO_x capacity is reached at 300–330 °C, an enhanced NO_x storage capacity compared to the first lean phase performed at 250 °C was observed (see Figure 11c). The amount of slipped NO_x during the rich phases was found to be strongly dependent on temperature. In order to compare the two LNTs regarding the NO_x slip, first the desorbing NO_x ($NO_{x,\mathrm{slip,r4}}$) was estimated under cycling steady-state conditions, i.e. during the rich phase following lean phase 4 and was calculated using equation Eq. 8. The temperature-dependent content of slipped NO_x compared to the stored NO_x ($NO_{x,\mathrm{st,c4}}$) at different rich phase durations evaluated by equation Eq. 9 are shown in Figure 14.

$$\mathrm{NO}_{x,\mathrm{slip,r4}}=\int\limits_{t_{\mathrm{s,r4}}}^{t_{\mathrm{e,r4}}} c_{\mathrm{NO}_{x,\mathrm{slip,r4}}}\mathrm{d}t \tag{8}$$

$$\frac{\mathrm{NO}_{x,\mathrm{slip,r4}}}{\mathrm{NO}_{x,\mathrm{st,c4}}}=\frac{\int_{t_{\mathrm{s,r4}}}^{t_{\mathrm{e,r4}}} c_{\mathrm{NO}_{x,\mathrm{slip,r4}}}\mathrm{d}t}{\mathrm{NO}_{x,\mathrm{st,c4}}} \tag{9}$$

Two main observations are apparent. First, only at 150 °C LNT 1 released a higher ratio of $NO_{x,\mathrm{slip,r4}}/NO_{x,\mathrm{st,c4}}$, but the total amount of NO_x slipped at this temperature from the catalyst during regeneration was very small (1–2 mmol/l). Second, at higher temperatures lower ratios of slipped NO_x below 20 %

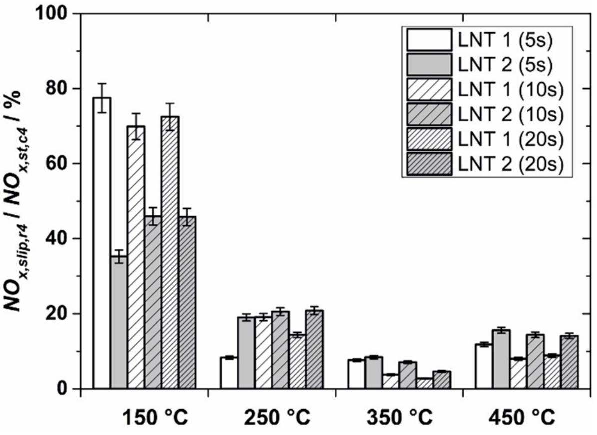

Figure 14. Temperature-dependent fraction of slipped NO_x for both LNTs during regeneration in cycle 4 at different rich phase durations.

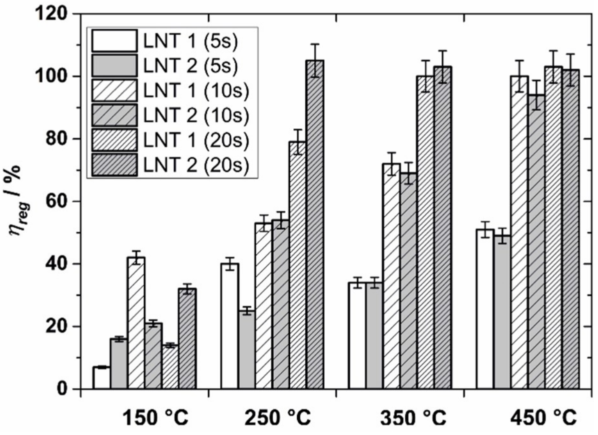

Figure 15. Comparison of the calculated regeneration efficiency η_{reg} at different temperatures and rich phase durations for LNT 1 and LNT 2.

were measured for both LNTs. The results could be explained by a consideration of the underlying processes. As shown in Figure 14, the rich phases are always accompanied by a temperature increase resulting mainly from the partial oxidation of the reducing agents. By that, part of the stored NO_x desorbs from the storage phase. Generally, at low temperatures ($\leq$ 250 °C), the speed of the NO_x reduction is too slow to reduce all of the desorbed NO_x, leading to a small slip of unreacted NO_x, while the increasing catalyst temperature during regeneration results in a higher storage capacity. At temperatures above 250 °C, the NO_x reduction speed is much faster so that the main part of the desorbed NO_x can still be reduced on the catalyst before slipping off, thus lowering the amount of downstream NO_x. At 450 °C the temperature increase results in a much faster decomposition of the stored nitrates which cannot be balanced by the higher reduction speed anymore. This leads to the observed increase of slipped NO_x.

Regeneration efficiency

As already mentioned, especially at low temperatures and short regeneration times, not all of the stored NO_x is reduced. The regeneration efficiency η_{reg} was determined to calculate the available NO_x storage capacity under steady-state conditions. Here, also the amount of NO_x slipped during the subsequent rich phase is considered, since it is stored in the LNTs, but is not regenerated in terms of reduction. The fifth and final cycle is followed by a thermal desorption phase without NO dosage. This allows a more accurate calculation of the slipped NO_x in the regeneration phase. Consequently, cycle 5 was used to calculate η_{reg} for certain temperatures and a certain regeneration duration according to Equation (10). The results are displayed in Figure 15.

$$\eta_{\text{reg}} = \frac{NO_{x,\text{st,c5}} - NO_{x,\text{slip,r5}}}{NO_{x,\text{st,c1}} - NO_{x,\text{slip,r1}}} \cdot 100\,\% \tag{10}$$

Three trends are clearly visible in evaluating η_{reg}. First, the regeneration efficiency of LNT 2 is significantly better for temperatures of 250 °C and below in the case of long regenerations times of 20 s. At higher temperatures of 350 °C and above, both LNTs showed comparable efficiencies within the accuracy of the measurements. Nevertheless, under certain conditions at low temperatures, (150 °C, 10 s regeneration and 250 °C, 5 s regeneration), LNT 1 performed better. Regarding the overall trends of η_{reg}, a second trend is visible: In most experiments, a rise of η_{reg} was achieved by a prolonged duration of the rich phase due to the high NO_x loading closed to saturation. Third and last observation is that η_{reg} increased massively with rising temperature. At 150 °C, efficiencies of about 7–40 % were calculated for both LNTs, at 250 °C 25–100 % of the stored NO_x was converted and at 450 °C a regeneration time of 10 s was sufficient to achieve $\eta_{reg} = 100\,\%$. Although these values are in line with the results shown in the previous sections, the differences in the material properties between the LNTs are not represented by the comparable storage behavior of the two catalysts. Additionally, with respect to realistic exhaust conditions, the regeneration performance of the tested LNTs at low temperatures is quite low. For coupling with downstream SCR catalysts and required lean phase durations over 120 s, long rich phase durations at lower temperatures or higher reductive concentration in the rich gas must applied for complete catalyst regeneration which increases the fuel penalty. Due to the limited specific NO_x storage capacities of modern LNTs, also the use of higher catalyst volumes could be a possible pathway to optimize the overall performance of a combined LNT-SCR systems.

Oxygen storage capacity

Another major aspect of modern LNTs is their oxygen storage capacity (OSC). It is not an essential requirement for the LNT, but is rather an "add-on" from the addition of Pt/CeO_2 implemented in the washcoat to increase the low-temperature

NO_x storage capacity and to enhance WGS activity below 300 °C. The OSC can significantly influence the regeneration efficiency on the LNT by additionally oxidizing the reductive during the initial phase of the regeneration. To evaluate this property for both LNTs, corresponding cycling experiments were carried out at four different temperatures. In opposite to the other measurements, these were performed under water-free conditions, due to the possible side reaction of CO with water to CO_2 via the water gas shift reaction (WGS). The results are shown in Figure 16.

As expected, the OSC increases for both catalysts with rising temperature. Generally, LNT 1 was found to have only 50–75 % of the OSC compared to LNT 2, although the determined concentration of Ce – which is mainly responsible for the OSC characteristics – in LNT 1 was 130 g/l and thus 20 % higher compared to LNT 2 (see Table 1). These contradictory results could have three reasons, which are not clarified by the characterization of the washcoat compositions: i) different intrinsic redox activity and enhancement of the redox potential by Pt or additives like La or Zr, ii) additional loading of $BaCO_3$ on the ceria of LNT 1 (see Figure 5 and Figure 7) covering the surface and reducing the contact between Pt and CeO_2, this can result in a lower redox activity in the washcoat, or iii) locating a part of the Pt/CeO_2 composite without any storage component in the top layer of LNT 2. However, from the catalytic point of view and with regard to the regeneration behavior, a lower OSC as in LNT 1 increases the reduction efficiency due to the lower consumption of the reductive during the initial phase of the regeneration.[66]

Gas composition during regeneration

Although both LNTs revealed very comparable NO_x storage behavior, during the catalytic tests, enormous differences in the regeneration performance of the two LNTs were observed. Figure 17 shows the downstream gas composition for the two LNTs during regeneration after lean phase 4 at 250 °C for different rich phase durations. For LNT 1 (Figure 17 A, B, C), irrespective of the overall regeneration time, a high CO slip was detected only 2 s after the beginning of the rich phase in parallel with a desorption of unreduced NO_x. A decrease of this desorption was observed at a regeneration time of 20 s, whereas in all other cases it remained constant until the end of regeneration. With rising regeneration time increasing NH_3 production of up to 650 ppm was also detected. Concentrations of H_2 and N_2O were negligibly small. The dosed C_3H_6 with a feed gas concentration of 1200 ppm left the LNT nearly completely unreacted. As expected, during a regeneration time of 10 s, the CO slip concentration of approx. 3200 ppm was higher compared to 5 s regeneration (2500 ppm) since the system was not able to reach the equilibrium state in 5 s and the slip concentration rose during the whole rich phase. After 10 s, a stable CO slip was reached. According to this assumption, the same or a slightly higher CO slip concentration was expected at 20 s. However, this was not the case since a CO slip of only approx. 2500 ppm was detected. Concurrently, the NO_x slip concentration was reduced from approx. 750 ppm at 10 s regeneration compared to $<$ 500 ppm at 20 s.

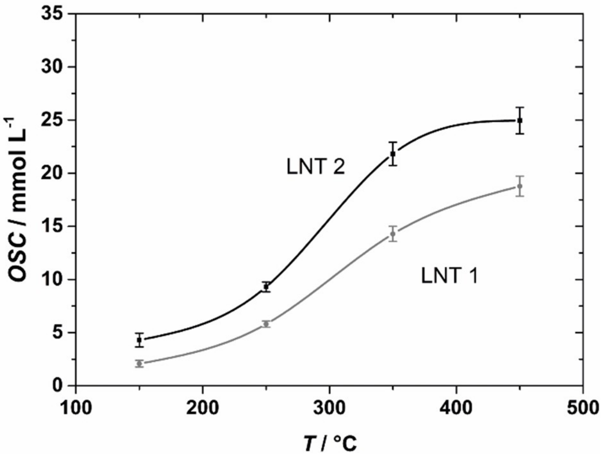

Figure 16. Temperature-dependent oxygen storage capacity of LNT 1 (grey line) and LNT 2 (black line).

Focusing on LNT 2 (Figure 17 D, E, F), a very different behavior compared to LNT 1 was observed. With LNT 2, immediately after the start of the rich phase, a strong N_2O production of up to 550 ppm (at 20 s regeneration) was observed, while at the same time a NO_x slip of approx. 1000 ppm was detected. The regeneration time of 5 s is difficult to evaluate due to the short rich phase leading to non-equilibrium conditions. The situation becomes clearer for the rich phase of 10 s. Here, the emission of NO_x and N_2O reached a maximum and then decreased in favor of a combined H_2/C_3H_6/CO/NH_3 emission of up to 50/800/1500/500 ppm, respectively. At a regeneration time of 20 s in particular, but also at 10 s, a short plateau concentration of all gases was observed before further following the described trend. Comparing the different regeneration times, besides continuation of regeneration, with rising regeneration time, again an unexpected trend for the NO_x slip was observed. Here, for 10 s regeneration time, the lowest concentration of 900 ppm was observed compared to 1100 ppm or 1000 ppm at rich phase durations of 5 s or 20 s.

These different observations could be explained by the different layer architecture of the washcoats and various active OSC materials in both catalysts. In terms of the N_2O evolution during regeneration, LNT 2 emitted the highest amounts directly after the transition from lean to rich and vice versa. This expected behavior was induced by the partial reduction of PtO_x to Pt(0) at the initial phase of the regeneration by the reductive, especially propylene. On these metallic Pt sites, gaseous NO released from the adsorption sites, can dissociate into N- and O-adatoms. These N-adsorbed species reacts subsequently with undissociated gaseous or stored NO to N_2O.[67] Generally, the amount of nitrous oxide released from the catalyst, was influenced by the temperature, the reduction speed of the PtO_x to metallic Pt and the type of the reductive. But it mainly depended on the local (CO, H_2, C_3H_6)/NO ratio inside the catalyst. Low temperatures ($\leq$ 250 °C) and low reductive concentrations near and on the catalytic surface lead to a slow NO

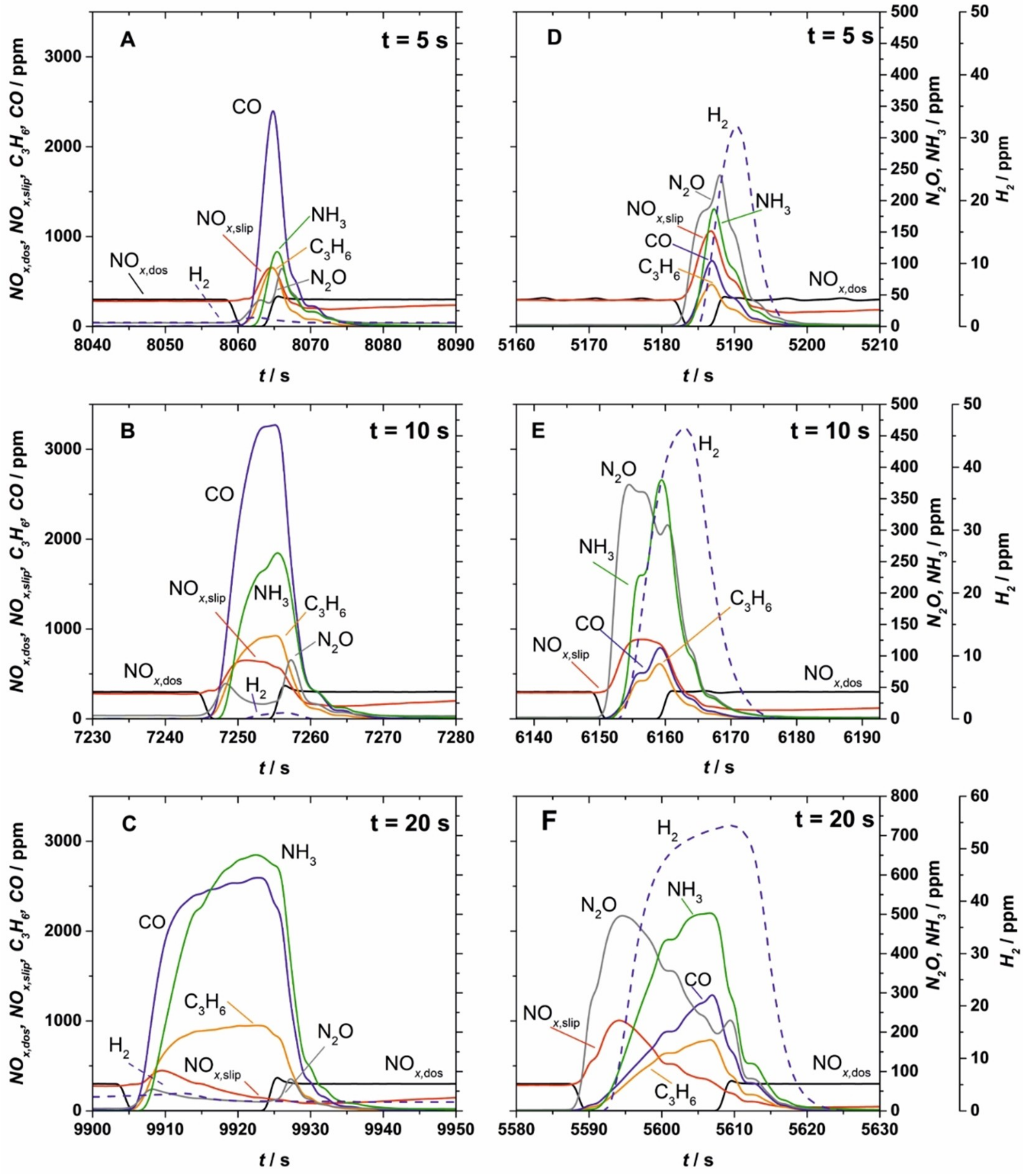

Figure 17. Evolution of the gas composition during regeneration at 250 °C of LNT 1 (A, B, C) and LNT 2 (D, E, F) at different rich phase durations of 5 s, 10 s and 20 s respectively.

reduction on the PGM sites and accordingly in a high N_2O emissions. In the case of LNT 2, this effect was reinforced by the OSC provided by higher ceria amounts. This highly active oxygen source within the catalyst in addition to the residual O_2 in the rich gas decreases the amount of reducing species available. As a consequence, a high emission of not fully reduced N_2O was found in the exhaust gas of LNT 2 at the beginning of the rich phase. With progressive regeneration time, the oxygen saturation of the ceria decreased and thus the amount of N_2O also declined. At the transition from rich to lean phase, both LNTs emitted minor amounts the nitrous oxides, due to the oxidative decomposition of intermediate isocyanate reaction species by NO/O_2 left at the catalyst surface after regeneration.[68]

This normal behavior in N_2O formation during cycling of LNTs was not observed at the rich phase of LNT 1. This could be explained by the different rhodium loading strategies in both LNTs. In LNT 2, the Rh was dispersed within the top layer together with the other precious metals. Whereas in LNT 1, the rhodium was highly concentrated in a small zirconia film below the zeolite layer, which is also a high active catalyst for the decomposition of N_2O under reducing conditions at low temperatures (200 to 400 °C). It reduces the nitrous oxides coming from the bottom layer with fresh regeneration gas.[69,70,71] At the transition from rich to lean, the metallic Rh was first oxidized with the lean gas to Rh_2O_3, which has a much lower activity to reduce N_2O, resulting in a small nitrous oxide slip.

Both LNTs emitted higher amounts of CO and C_3H_6 with continuing regeneration time due to the decreasing oxygen disposability of the OSC material. Compared to LNT 1, minor amounts of unreacted CO and higher concentrations of unreacted H_2 breakthrough occurred with LNT 2. This could be explained by the higher WGS activity of the Pt/CeO_2 in LNT 2 at this temperature, which is also caused by the higher redox activity of the OSC material. As a result, for LNT 1 with a less active ceria phase, an enormous CO slip and high C_3H_6 emissions were observed during regeneration. Nevertheless, a WGS reaction proceeds on the catalyst leading to H_2 formation. In comparison to LNT 2, the H_2 slip is close to the detection limit, but the emission of NH_3 is only 40% lower (5 s rich phase) or even higher (20 s rich phase). This difference may be caused by rate-limiting H_2 production or by more efficient NO_x-reducing sites, e.g. Pt. For the same reason, the differences in the ammonia evolution could be explained. For LNT 1 with lower OSC, the NH_3 release starts directly after CO breakthrough, whereas in LNT 2 with higher OSC, the ammonia formation begins delayed after the reductive/NO ratio leads a suitable value for the complete reduction of the adsorbed NO_x. This is due to the additional consumption of the reductive at the beginning of the regeneration caused by the higher OSC.

Comparing the two LNTs concerning NO_x slip, it was found that LNT 2 showed significantly higher values. This can be explained by the higher catalyst temperature (see Figure 12) caused from the exothermal oxidation of the reducing agents by the more active OSC material in LNT 2 and the higher WGS activity. The results also imply that, due to the lower reductant slip, LNT 2 displays better NO_x reducing performance. However, this was contradicted by the NO_x storage measurements previously evaluated. The higher consumption of reductive is only caused by the direct oxidation.

These results demonstrate that the material properties of the used ceria compounds in the washcoats in terms of the OSC, WGS activity and layer architecture have a negligible influence on the storage efficiency. On the contrary, they greatly affect the regeneration behavior of the LNTs. High yields of ammonia during regeneration for further use in a downstream SCR catalyst can only be reached, when the OSC is as low as possible. In parallel, a high WGS activity must be implemented in the washcoat to prevent CO slip at low temperatures. This cannot be realized with Pt/CeO_2 for such an application. However, the separation of the storage compounds and the regeneration supporting materials in separate layers is beneficial to improve the performance.

To complete the investigations on the composition of the exhaust gas in the rich phase, the results from 150 °C, 350 °C and 450 °C at 10 s regeneration time were also considered (Figure 18). At low temperatures like 150 °C there is hardly any reduction of the adsorbed NO_x. This was proven by the slip of 11000 ppm CO, 3500 ppm H_2 and 1100 ppm C_3H_6 for both LNTs, which almost rises to the dosed concentrations of 500 ppm. For LNT 2, minor concentrations of 10–15 ppm N_2O and NH_3 were detected, but they are negligibly low. At 350 °C, also for LNT 1, N_2O emission is observed at the beginning of regeneration, followed by a CO and H_2 slip that is accompanied by a strong NH_3 slip. Compared to 250 °C, the CO slip is minimized to 800 ppm, whereas the slipped H_2 displayed significantly higher concentrations. LNT 2 showed comparable behavior up to 250 °C, but with lower N_2O production and a more than tenfold H_2 slip. Additionally, NH_3 emissions were reduced from 400 ppm to 100 ppm and CO was reduced to 400 ppm. In contrast to 250 °C, both LNTs reacted most of the dosed C_3H_6, which was not the case at 250 °C. The slipped NO_x was barely affected, only a small decrease by less than 100 ppm was found.

At high temperatures of about 450 °C, irrespective of the LNT, enormous concentrations of H_2 in the range of 5000 ppm were detected. Moreover, for both catalysts hardly any N_2O emissions or C_3H_6 slip occurred. For LNT 1, comparable low NH_3 emissions of approx. 280 ppm were measured, whereas CO and NO_x slip were hardly changed at all. The same was true for LNT 2: Here hardly any changes besides the H_2 concentrations were observed compared to 350 °C.

These results also yield some interesting findings. First, the low-temperature activity of both LNTs in terms of NO_x storage leads to low N_2O and NH_3 emissions at 150 °C. Nevertheless, the high CO, H_2 and C_3H_6 slip near to the initial concentration of the rich gas was unexpected, since the light-off temperatures for the oxidation of these reductive on Pt is known to be between 100 and 150 °C under lean conditions. As a concentration of 6000 ppm O_2 was present in the exhaust gas, at least a significant portion of the hydrogen must be oxidized at these temperatures on both LNTs. The observed behavior will be object of further research.

The results at 350 °C also reveal that for LNT 1 the same OSC behavior as in LNT 2 can be found – mainly an oxidation of the reducing agent at the lean-rich transition leading to N_2O emissions and subsequent $H_2/CO/NH_3$ emissions after the oxygen disposability of the OSC material decreases with rising regeneration time. The oxidation of the reducing agent is also represented by a rise of the catalyst core temperature by about 95 °C (Figure 19). This result is additional evidence for the reduced activity of the Pt/CeO_2 phase in LNT 1 compared to LNT 2, as it catalyzed the same reactions but at higher temperatures. LNT 2 itself demonstrated a higher influence of the WGS reaction at this temperature compared to 250 °C, leading to sufficient H_2 supply, which is represented by a relatively high H_2 slip. Together with a high NO_x reduction performance, N_2O emissions are reduced to less than 100 ppm. The low emissions of NH_3 under these conditions can be explained by an oxidation reaction with the O_2 present in the gas stream or by in situ consumption as an additional reductive for NO_x. At this temperature, both LNTs are able to use the C_3H_6 as a reducing agent. Interestingly, the NO_x slip at the start of the reaction was only changed to a minor degree.

The situation at 450 °C involves an additional reaction leading to high H_2 concentrations. At this temperature, the steam reforming of propylene into H_2 and CO takes place according to Equation (11). Moreover, the endothermicity of the reaction leads to a lower catalyst temperature increase compared to the performance test at 250 °C (Figure 19).

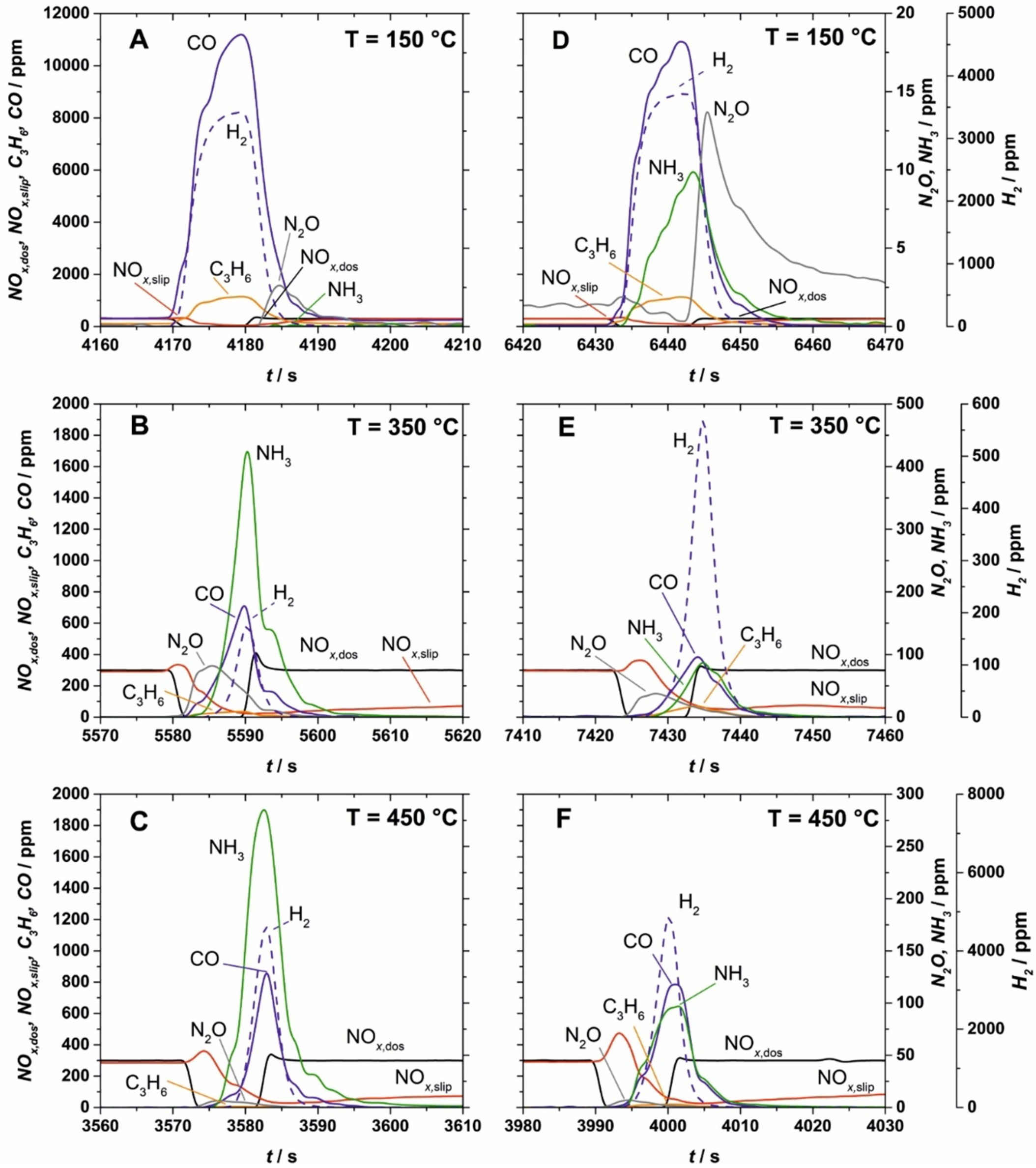

Figure 18. Evolution of the gas composition during regeneration with a rich phase duration of 10 s for LNT 1 (A,B,C) and LNT 2 (D,E,F) at different temperatures.

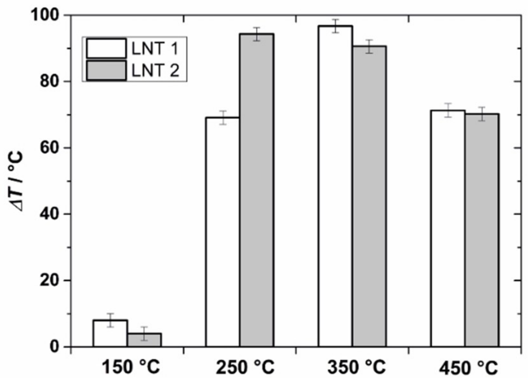

Figure 19. Differences between the lean phase and the regeneration temperature (T2) inside LNT 1 and LNT 2 at a rich phase duration of 10 s.

$$C_3H_6 + 3\ H_2O \rightleftharpoons\ 6\ H_2 + 3\ CO \tag{11}$$

The reaction was obviously better catalyzed by LNT 2, resulting in a stronger increase of H_2 and CO slip. In comparison to 350 °C, no major differences were found in the exhaust gas. In contrast to LNT 2, LNT 1 seems to benefit from the increased reductive concentration due to the significantly higher reducing efficiency of LNT 1 compared to 350 °C, while detected concentrations of slipped species were not changed.

NH_3- and N_2O-selectivities during regeneration

For a final evaluation concerning the suitability of both LNTs for coupling with a downstream SCR system the NH_3- and N_2O-

selectivities were estimated under steady-state conditions during the rich phase following lean phase 4 and calculated using Equations (12) and (13). The temperature-dependent content of slipped NH_3 and N_2O compared to the stored NO_x ($NO_{x,st,c4}$) at different rich phase durations are shown in Figure 20 and Figure 21.

$$\frac{\mathrm{NH}_{3,\mathrm{slip,r4}}}{\mathrm{NO}_{x,\mathrm{st,c4}}} = \frac{\int_{t_{\mathrm{s,r4}}}^{t_{\mathrm{e,r4}}} c_{\mathrm{NH}_{3,\mathrm{slip,r4}}}\,\mathrm{d}t}{\mathrm{NO}_{x,\mathrm{st,c4}}} \tag{12}$$

$$\frac{\mathrm{N}_2\mathrm{O}_{\mathrm{slip,r4}}}{\mathrm{NO}_{x,\mathrm{st,c4}}} = \frac{\int_{t_{\mathrm{s,r4}}}^{t_{\mathrm{e,r4}}} c_{\mathrm{N}_2\mathrm{O}_{\mathrm{slip,r4}}}\,\mathrm{d}t}{\mathrm{NO}_{x,\mathrm{st,c4}}} \tag{13}$$

Generally, the fraction of the slipped ammonia increases with rising regeneration time for both LNTs at all investigated temperatures. Except for 150 °C, LNT 1 generates more NH_3 than LNT 2. It also reaches a maximum of nearly 25% of the emitted N-containing gas species at 250 °C with a rich phase duration of 20 s. This trend was also observed at higher temperatures but with lower yields of ammonia due to the increasing consumption by oxidation (residual O_2 in the rich gas) and reduction of the stored NO_x.

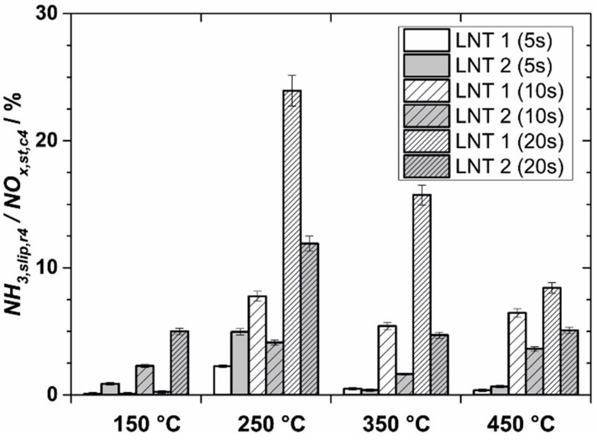

Figure 20. Temperature-dependent fraction of slipped NH_3 for both LNTs during regeneration in cycle 4 at three different rich phase durations.

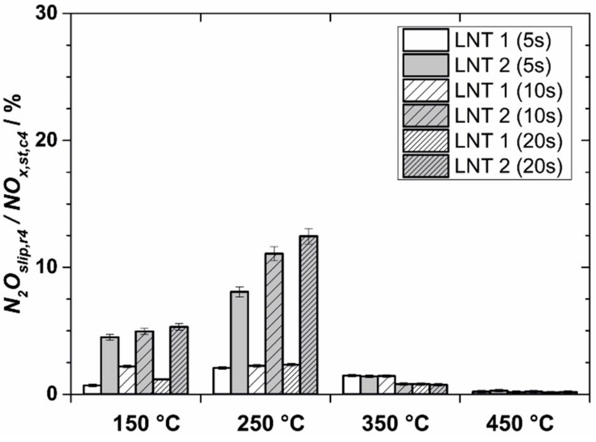

Figure 21. Temperature-dependent fraction of slipped N_2O for both LNTs during regeneration in cycle 4 at three different rich phase durations.

Comparing the N_2O selectivity of both LNTs during regeneration, only for LNT 2 a remarkable nitrous oxide emission could be found at temperatures up to 250 °C, which reaches 13% at a rich phase duration of 20 s. At temperatures higher than 250 °C, the nitrous oxide amount in the rich gas was negligibly low. In terms of the observed NH_3 and N_2O emissions LNT 1 seems to be an acceptable candidate for coupling with downstream SCR catalysts. For further improvement of the ammonia yield during regeneration mainly higher reductive concentrations in the rich gas event should be applied to increase the local reductive/NO ratio inside the catalyst. This will result in an enhanced activity for total reduction of the stored NO_x.

Conclusions

In this study, two commercially available lean NO_x trap catalysts (LNTs) were investigated in terms of washcoat composition and catalytic properties to assess their performance for future coupling with SCR catalysts. For such an application, a LNT has to fulfill several requirements. Besides a high storage capacity, especially during long lean phases at temperatures below 250 °C, a high NH_3 selectivity during regeneration as a reductive for the slipped NO_x in a downstream SCR catalyst is also crucial. Both LNTs revealed the same NO_x storage materials, namely PGM loaded ceria, $BaCO_3$ and $MgAl_2O_4$ phases, but with different amounts and distributions within the washcoats in layered structures. They were analyzed in lean-rich cycle experiments under realistic gas compositions and higher NO_x loadings on a laboratory gas test bench. Both catalysts showed comparable and reproducible NO_x storage capacities with an estimated maximum of around 42 mmol/l at 300 °C, but with fundamental different gas compositions during regeneration. Generally, it was found that the storage efficiencies decrease down to around 40% after a lean phase duration of 100 s at temperatures below 250 °C resulting in a high NO_x slip. Additionally, rich phase durations longer than 10 s are necessary at higher NO_x loadings to drain the LNTs completely. This corresponds with a NO_x slip during regeneration, which is mainly caused by the reaction of the reductives with the residual oxygen in the rich gas, which increases the catalyst temperature rapidly. Further optimization of combined LNT-SCR systems has to address these findings by using low temperature high storage materials in the washcoat and by increasing the reductive concentration during short rich purges to extent the lean phases by low NO_x emissions.

In terms of the gas composition during regeneration, both LNTs showed different NH_3 and N_2O selectivity caused by the different layer architectures and the redox activities of the ceria in the washcoats. For LNT 1 with a thin Rh containing separate layer, the generation of N_2O can be reduced to a minimum in parallel with a higher amount of ammonia of up to 25% at 250 °C compared to LNT 2 with a higher OSC. In contrast, the

CO slip of LNT 1 is much higher at low temperatures. This is due to the higher WGS activity of LNT 2. In this catalyst the Pt/CeO_2 was located separately from the storage materials in a top layer, which could be the reason for this enhanced functionality.

As a final assessment, LNT 1 seems to be more suitable for the desired application with respect to its higher NH_3 selectivity and lower N_2O emission during regeneration, but the composition and the performance could be still optimized. Even if not all questions about the composition/ performance correlations of LNTs have yet been answered by performance investigation on a laboratory gas test bench, some indications to improve the properties of current LNTs can be given. Besides the implementation of new components with superior low temperature NO_x storage capacity, the independent tuning of OSC and WGS functionalities play a key role in developing high-performance LNT catalysts. This could not be realized with platinized ceria inside the washcoat. In addition, a new WGS catalyst should be implemented in a layered washcoat structure. One possibility is a three-layer architecture with a bottom layer containing the storage materials, a middle layer with WGS functionality and a highly active oxidation catalyst to reduce hydrocarbon and CO emissions during lean phases and a Rh containing top layer to improve the regeneration behavior. In this way, N_2O and CO emissions could be reduced to a minimum and the ammonia yield could be maximized during regeneration, which enhances the possibility to achieve the best LNT-SCR performance. For such optimizations, the NH_3 storage capacity of the downstream SCR catalyst at certain regeneration temperatures as well as the ratio between the generated amount of ammonia and slipped NO_x during lean and rich phase must be considered to maximize the overall N_2 selectivity. Therefore, individual lean rich cycling durations and rich gas compositions in relation to the NO_x raw emission, exhaust temperature and fuel penalty must be found for a suitable engine control strategy. Due to this complex coherence, an optimum ammonia selectivity during regeneration cannot be proposed as the only key factor for LNTs to be suitable in a coupled system.

Experimental Section

Catalyst characterization

Fully canned LNT catalysts were obtained from two different vehicles. LNT 1 was taken from vehicle 1 with a 1598 cm^3 diesel engine (60.1 kW/l nominal specific power). It consisted of a ceramic honeycomb monolith with a diameter of 17.2 cm and a length of 8.2 cm ($V_{LNT\,1}=1905\ cm^3$). LNT 2 was taken from vehicle 2 with a 1968 cm^3 diesel engine (68.6 kW/l nominal specific power). It was based on a metal foil monolith with a diameter of 11.5 cm and a length of 13.8 cm ($V_{LNT\,2}=1433\ cm^3$). The catalyst cannings were removed to obtain the samples for detailed analyses and performance tests. LNT 2 was then completely embedded in pure ash-free hard wax before sawing in order to prevent washcoat delaminating during the preparation process. Subsequently, each LNT 2 specimen was de-waxed by Soxhlet extraction with hexane followed by calcination at 600 °C for 5 h under air. The samples from the full ceramic LNT 1 were easily prepared by core drilling. The catalytic measurements were carried out on a rectangular sample of LNT 2 with a length of 13.8 cm, a width of 1.78 cm and a height of 1.78 cm and on a cylindrical specimen of LNT 1 with a length of 8.2 cm and a diameter of 1.85 cm, respectively.

Each sample was fixed in a titanium canning using a mounting mat which was subsequently hydrothermally aged for 10 h in a furnace at 750 °C in an atmosphere of 10% H_2O in air before use. For ICP-OES analyses, 1/8 slices of the catalyst were first milled and homogenized with SiN tools and further dissolved in HNO_3/HCl or HNO_3/HCl/HF using a high pressure microwave system. Analyses were performed with an ICAP 6500 (Thermo Fisher Scientific, Waltham, MA, USA). The specific element compositions per liter catalyst volume were calculated from these results.

For cross section SEM measurements, the catalyst samples were embedded in epoxy resin, polished and carbon-coated by thermal deposition. SEM analyses were carried out on a Zeiss Merlin FEG-SEM (Carl Zeiss Microscopy GmbH, Oberkochen, Germany) with an acceleration voltage of 10 kV and a backscattered-electron detector (BSE). Element mappings by EDX were recorded by means of an integrated Aztec, X-Max 150 SDD Detector (Oxford Instruments Nanotechnology, High Wycombe, UK). Particle size evaluation was performed with the software ImageJ.

Investigations at higher magnification were performed by transmission electron microscopy using a 200 kV LIBRA 200FE (Carl Zeiss Microscopy GmbH, Oberkochen, Germany) equipped with an EDX (Bruker AXS GmbH, Karlsruhe, Germany) and high-angle annular dark-field (HAADF) detector (E.A. Fischione Instruments, Inc., Export, PA, USA). Electron transparent lamella of the samples for TEM investigation were obtained by focused ion beam machining (FIB) using a Strata 205 from FEI company (Hillsboro, OR, USA).

To identify the active components within the catalysts, the phase compositions of the washcoats were determined by X-ray diffraction, using Cu Kα radiation (D4 Endeavor, Bruker). For that purpose, the washcoats were peeled off the surface of the monoliths.

Catalytic performance measurements

Experimental setup

The catalytic performance measurements were carried out on a laboratory gas test bench (LGB) where all pipes are manufactured from grade 2 titanium (Figure 22). The reaction gases were mixed from gas bottles with nitrogen as a balance to obtain a constant space velocity throughout the test. N_2, O_2 (both purity $\geq$ 99.999%) and CO_2 (purity $\geq$ 99.5%) were used as bulk gases. All other gases were mixtures of the respective species in N_2 with 9% for CO, 1% for C_3H_6 and for NO, as well as 10% for H_2, respectively. Water vapor was generated using a HovaPOR LF-1200 (IAS GmbH, Oberursel, Germany) with part of the N_2 flow. All gas flows were subjected to closed-loop control by high dynamic mass flow controllers (MFC) type SLA5850 from Brooks Instrument, LLC (Hatfield, PA, USA). Downstream of each MFC a normally closed, direct-acting solenoid 2/2-way valve (type 0330, Christian Bürkert GmbH & Co. KG, Ingelfingen, Germany) was mounted to assure fast cut-off of gas flow when no flow is requested and to avoid leakage flow over the MFC. The heating unit consisted of two separate lines for inert and reaction gases. The temperature-sensitive reactive gases were only heated convectively to 190 °C and mixed close to the reactor with the inert gases. The temperature of the mixed gas was subjected to closed-loop control by heating the inert gases using two preheaters and one main heater (heating unit in Figure 22A).

The reactor unit containing the catalyst sample in a titanium canning was mounted inside a well-insulated reactor that was

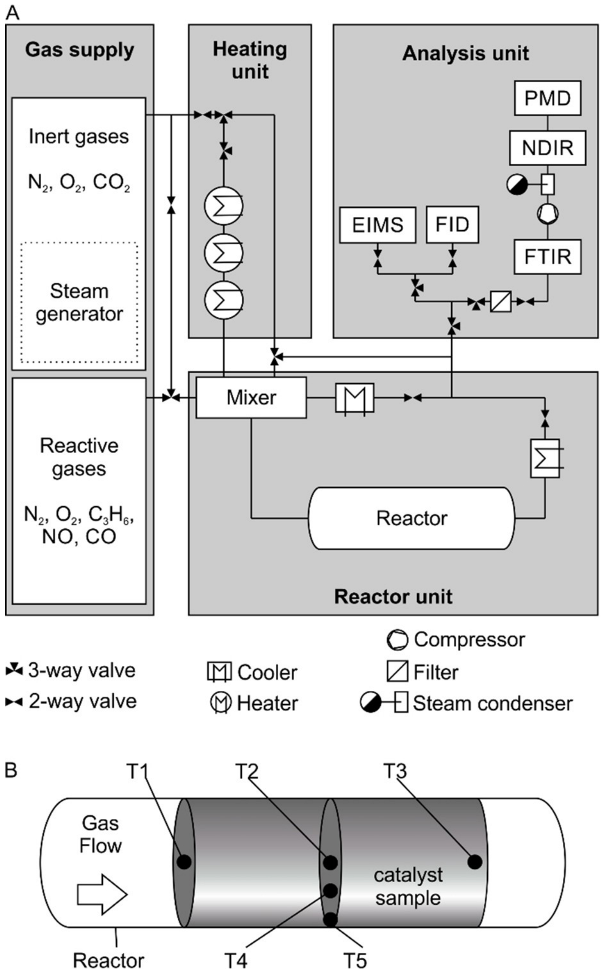

Figure 22. A: Schematic of the laboratory gas test bench (LGB). B: Positions of the thermocouples T1–T5 in the catalyst sample.

equipped with an additional electric heater to compensate thermal loss. The temperature set-points of the furnace heater were coupled to the set-points of the pre-heaters and main heaters. Five thermocouples (type K) were mounted in each catalyst to determine the temperature distribution throughout the catalyst during the experiments (Figure 22B). They were positioned in a radial direction in the middle of the sample 1 cm downstream of the inlet (T1), half way between the inlet and outlet (T2) and 1 cm upstream of the outlet (T3); furthermore, half way between the inlet and outlet at half radius (T4) and at one of the outer channels (T5). The mean catalyst temperature refers to the arithmetic mean of these five temperatures

The analytic unit measured either the gas composition upstream or downstream of the catalyst. The gas flow was split into four different lines: In the first line, the H_2 content was measured by an electron-ionization mass spectrometer (EIMS) of the type H-Sense supplied by MS4-Analysentechnik (Rockenberg, Germany). In the second line, the total amount of hydrocarbons was evaluated by a flame-ionization detector (FID), Thermo-FID MP of SK-Elektronik GmbH (Leverkusen, Germany). The third line was connected to a Fourier transform infrared spectrometer (FTIR) MultiGas 2030 supplied by MKS Instruments, Inc. (Andover, MA, USA) to analyze H_2O, CO, CO_2, NO, NO_2, N_2O, NH_3, C_3H_6 and C_3H_8 at 191 °C. The outlet of the FTIR was connected to a condenser to separate the water from the analysis gas, which was then fed into a combined measurement system from FEV Europe GmbH (Aachen, Germany) including a non-dispersive infrared spectrometer (NDIR) for CO and CO_2 measurement and a paramagnetic detector (PMD) for O_2 detection. In the later evaluation, the CO signal from the FTIR and the CO_2 signal of the NDIR were used. The other measurement equipment was used for a plausibility check. The fourth line was connected to the exhaust via a needle valve allowing the flow into the measurement equipment to be adjusted and thus the pressure in the FTIR gas cell. All measurement data was evaluated with a frequency of 1 Hz.

Lean-rich-cycle experiments

Lean-rich-cycle experiments at a constant gas hourly space velocity (GHSV) of 60000 h^{-1} were performed on the laboratory gas test bench to obtain results comparable to vehicle operation of the LNTs at $\lambda = 1.526$. The lean gas composition contained 8 °% O_2, 300 ppm NO, 100 ppm C_3H_6 as a representative hydrocarbon, and 500 ppm CO. The rich gas composition represents a realistic lambda situation of 0.983 during regeneration with a residual O_2 content of 6000 ppm and 12000 ppm CO, 1200 ppm C_3H_6 and 4000 ppm H_2 as reduction species. The conditions for NO_x storage-regeneration cycling experiments are summarized in Table 4. A separate set of MFCs was used for lean and rich conditions, respectively. The switching from lean to rich (and vice versa) is achieved by closing the solenoid 2/2-way valves of the respective MFCs for the first mixture and setting the corresponding set voltages to zero, while at the same time opening the solenoid 2/2-way valves and setting the desired voltage of the MFC for the second mixture. The change in N_2 balance mass flow was set by adjusting the respective MFC voltage. This procedure guarantee a fast transition between lean and rich conditions, where the respective gas compositions reaches their equilibrium within 1.5 s. The catalyst was conditioned prior to each test for 5 min at 500 °C with a typical rich gas mixture of 12000 ppm CO, 4000 ppm H_2, 10% CO_2 and 10% H_2O in N_2 to ensure a NO_x-free washcoat before the measurements. The cycling experiments were carried out at 150, 250, 350 and 450 °C, respectively, and consisted of five cycles, where each cycle was composed of a lean and a rich phase. In preliminary tests, the durations of the lean phases at each temperature were determined for both catalysts until a NO_x slip of at least 90% was observed to ensure comparable NO_x loading situations. The longest duration at each temperature was then chosen for the experiments. For example, the lean event duration of 900 s at 250 °C was adjusted due to the maximum NO_x storage capacity at this temperature. At each temperature, three experiments were carried out with different rich phase durations of 5, 10 and 20 s, respectively. Hence, twelve experiments were performed per catalyst. After the last cycle of each experiment, the atmosphere was changed to 10% H_2O in nitrogen and the temperature was increased rapidly with a heating ramp of 60 K/min up to 500 °C to evaluate the amount of NO_x remaining in the catalyst after the last rich phase. This was followed by a conditioning step of 5 min with the above-mentioned typical rich gas mixture.

Oxygen storage measurements

The oxygen storage capacity of both catalysts was determined at a constant GHSV of 60000 h^{-1} under dry conditions at four different temperatures of 150, 250, 350 and 450 °C. The experimental conditions for the OSC storage cycling experiments are given in Table 5.

The catalysts were conditioned prior to each test at 500 °C for 5 min with 2% CO in N_2. The test procedure consisted of ten cycles with four phases and was performed at each temperature. In the first

Table 5. Conditions used for OSC storage cycling experiments at GHSV = 60000 h-1, gases were balanced with N_2

Parameter	Lean	Rich
Duration [s]	30	60
Temperature [°C]	150/250/350/450	150/250/350/450
CO [%]	0	2
O_2 [%]	1	0

lean phase with 1% O_2 in nitrogen and a duration of 30 s, the oxygen storage material in the catalyst was re-oxidized followed by a purging phase of 30 s with pure N_2 to remove residual O_2 from the reactor atmosphere. Subsequently, the OSC components were reduced in the rich phase for 60 s with 2% CO in N_2. Finally, the residual CO was purged out of the reactor for 60 s with pure nitrogen prior to the next cycle. The OSC was calculated based on the CO_2 formed during the rich phase according to [Eq. (14)].[72,73,74]

$$\mathrm{OSC} = 2 \cdot \int_{t_1}^{t_2} c_{\mathrm{CO_2}}\,\mathrm{d}t \tag{14}$$

Acknowledgements

We gratefully acknowledge funding by the Excellence Initiative of the German federal and state Governments (ERS Seed Fund, funding of the project house „Center for Automotive Catalytic Systems Aachen" ACA, and large scale equipment). For funding the Center for Mobile Propulsion and its equipment that enabled these investigations we thank the German Research Foundation (DFG) and the Wissenschaftsrat. We thank Mikroanalytisches Labor Pascher, Remagen, Germany for performing ICP-OES investigations. Open access funding enabled and organized by Projekt DEAL.

Conflict of Interest

The authors declare no conflict of interest.

Keywords: Supported catalyst · Nitrogen oxides · lean NO_x trap (LNT) · selective catalytic reduction (SCR) · LNT-SCR catalyst

[1] E. Lox, *Handbook of Heterogeneous Catalysis*, Vol. 5 (Eds. G. Ertl, H. Knözinger, F. Schüth, J. Weitkamp), Wiley-VHC Verlag GmbH & Co. KGaA, Weinheim, **2008**, pp. 2274–2345.
[2] D. Gruden, *Umweltschutz in der Automobilindustrie*, Vieweg + Teubner, Wiesbaden, **2008**, p. 413.
[3] K. Mollenhauer, K. Schreiner, *Handbook of diesel engines, (Eds.: K. Mollenhauer, H. Tschoeke)*, Springer Science & Business Media, Berlin, **2010**, pp. 3–30.
[4] U. S. Government Printing Office (Eds.), "An Act to improve, strengthen and accelerate programs for the prevention and abatement of air pollution," in Public Law 88–206, Washington **1963**.
[5] Europäisches Parlament, Rat der Europäischen Union in Verordnung (EU) Nr. 168/2013 des Europäischen Parlaments und Rates vom 15. Januar 2013 über die Genehmigung und Marktüberwachung von zwei- oder dreirädrigen und vierrädrigen Fahrzeugen, Amtsblatt der Europäischen Gemeinschaften **2016**, pp. 52–128.
[6] S. Brandenberger, O. Kröcher, A. Tissler, R. Althoff, *Catal. Rev.* **2008**, *50*, 492–531.
[7] W.-P. Trautwein, *AdBlue als Reduktionsmittel für die Absenkung der NOx-Emissionen aus Nutzfahrzeugen mit Dieselmotor Teil 1*, DGMK, Hamburg **2003**, p. 29.
[8] H. Fang, H. DaCosta, *Appl. Catal. B* **2003**, *46*, 17–34.
[9] I. Nova, L. Castolid, L. T. E. Lietti, P. Forzatti, F. Prinetto, G. Ghiotti, *J. Catal.* **2004**, *222*, 377–388.
[10] E. Fridell, M. Skoglundh, B. Westberg, S. Johansson, G. Smedler, *J. Catal.* **1999**, *183*, 196–209.
[11] L. Lietti, P. Forzatti, I. Nova, E. Tronconi, *J. Catal.* **2001**, *204*, 175–191.
[12] L. Kubiak, L. Castolid, L. Lietti, S. Andonova, L. Olsson, *Catalysts* **2016**, *6*, 46.
[13] C. DiGiulio, J. Pihl, J.-S. Choi, J. Parks, M. Lance, T. Toops, M. Amiridis, *Appl. Catal. B* **2014**, *147*, 698–710.
[14] C. Boerensen, D. Roemer, C. Nederlof, E. Smirnov, F. Linzen, F. Goebel, B. Carberry, *SAE Int. J. Fuels Lubr.* **2017**, *10*.
[15] O. Bhardwaj, K. Krishnamurthy, D. Blanco, B. Holderbaum, T. Körfer, *SAE [Tech. Pap.]* **2017**.
[16] N. Miyoshi, S. Matsumoto, K. Katoh, T. Tanaka, J. Harada, N. Takahashi, K. Yokota, M. Sugiura, K. Kasahara, *SAE [Tech. Pap.]* **1995**.
[17] H. Tschoeke, A. Graf, J. Stein, M. Krüger, J. Schaller, N. Breuer, K. Engeljehringer, W. Schindler, in *Handbook of Diesel Engines, (Eds.: K. Mollenhauer, H. Tschoeke)*, Springer Science & Business Media, Berlin, **2010**, pp. 417–485.
[18] L. Lietti, N. Artioli, L. Righini, L. Castolid, P. Forzatti, *Ind. Eng. Chem. Res.* **2012**, *51*, 7597–7605.
[19] Nova, L. Lietti, P. Forzatti, *Catal. Today* **2008**, *136*, 128–135.
[20] Y. Renn, M. Harold, *ACS Catal.* **2011**, *1*, 969–988.
[21] H. Mahzoul, J. Brilhac, P. Gilot, *Appl. Catal. B* **1999**, *22*, L241–L248.
[22] P. Engström, A. Amberntsson, M. Skoglundh, E. Fridell, G. Smedler, *Appl. Catal. B* **1999**, *22*, 47–55.
[23] S. Roy, A. Baiker, *Chem. Rev.* **2009**, *109*, 4054–4091.
[24] X. Wei, X. Liu, M. Deeba, *Appl. Catal. B* **2005**, *58*, 41–49.
[25] S. Salsac, S. M. E. Fridell, *Appl. Catal. B* **2002**, *36*, 145–160.
[26] Y. Ji, T. Toops, U. Graham, G. Jacobs, M. Crocker, *Catal. Lett.* **2006**, *110*, 29–37.
[27] S. Philipp, A. Drochner, J. Kunert, H. Vogel, J. Theis, E. Lox, *Top. Catal.* **2004**, *30*, 235–238.
[28] M. Haneda, T. Morita, Y. Nagao, Y. Kintaichi, H. Hamada, *Phys. Chem. Chem. Phys.* **2001**, *3*, 4696–4700.
[29] Y. Ji, J.-S. Choi, T. Toops, M. Crocker, M. Naseri, *Catal. Today* **2008**, *136*, 146–155.
[30] A. Phatak, N. Koryabkina, S. Rai, J. Ratts, W. Ruettinger, R. Farrauto, G. Blau, W. Delgass, F. Rebeiro, *Catal. Today* **2007**, *123*, 224–234.
[31] T. Bunluesin, R. Gorte, G. Graham, *Appl. Catal. B* **1998**, *15*, 107–114.
[32] T. Szailer, J. Kwak, D. Kim, J. Hanson, C. Peden, J. Szanyi, *J. Catal.* **2006**, *239*, 51–64.
[33] J.-Y. Luo, W. Epling, G. Qi, W. Li, *Catal. Lett.* **2012**, *142*, 946–958.
[34] C. Shi, Y. Ji, U. Graham, G. Jacobs, M. Crocker, Z. Zhang, Y. Wang, T. Toops, *Appl. Catal. B* **2012**, *119*, 183–196.
[35] G. Fornasari, F. Trifiro, A. Vaccari, F. Prinetto, G. Ghiotti, G. Centi, *Catal. Today* **2002**, *75*, 421–429.
[36] S. Park, H. Ahn, I. Heo, I.-S. Nam, H. Lee, Y. Youn, H. Kim, *Top. Catal.* **2010**, *53*, 57–63.
[37] G. Centi, G. Fornasari, C. Gobbi, M. Livi, F. Trifiro, A. Vaccari, *Catal. Today* **2002**, *73*, 287–296.
[38] M. Takeuchi, S. Matsumoto, *Top. Catal.* **2004**, *28*, 151–156.
[39] J. Theis, J. Ura, R. McCabe, *SAE [Tech. Pap.]* **2007**.
[40] I. Hachisuka, H. Hirata, Y. Ikeda, S. Matsumoto, *SAE [Tech. Pap.]* **2000**.
[41] T. Johnson, *SAE Int. J. Fuels Lubr.* **2010**, *3*, 16–29.
[42] C. Menne, M. Rupp, D. Blanco-Rodriguez, B. Holderbaum, K. Krishnamurthy, T. Körfer, L. Ruwisch, A. Scheuer, *25th Aachen Colloquium Automobile and Engine Technology 2016*, Aachen, Germany, 2016.
[43] D. Blanco-Rodriguez, G. Vagnoni, B. Holderbaum, 8th IFAC Symposium on Advances in Automotive control (AAC), Norrköping, Sweden, 2016.
[44] T. Wittka, B. Holderbaum, B. Lüers, T. Körfer, 22nd Aachen Colloquium Automobile and Engine Technology 2013, Aachen, Germany, 2013.
[45] T. Wittka, B. Holderbaum, *Combust. Engines* **2014**, 68–76, 157.
[46] T. Körfer, W. Bick, B. Holderbaum, T. Wittka, *SIA Tech. Pap.* **2014**.
[47] J. R. González-Velasco, B. Pereda-Ayo, U. De-La-Torre, M. L.-F. R. Urrutxua, *ChemCatChem* **2018**, *10*, 2928–2940.
[48] U. De La Torre, M. Urrutxua, B. Pereda-Ayo, J. R. González-Velasco, *Catal. Today* **2017**, *60*, 30–39.
[49] T. Wittka, B. Holderbaum, P. Dittmann, S. Pischinger, *Emiss. Control Sci. Technol.* **2015**, *2*, 167–182.
[50] T. Maunula, *Combust. Engines* **2014**.

[51] J. Wang, Y. Ji, Z. He, M. Crocker, M. Dearth, R. W. McCabe, *Appl. Catal. B* **2012**, *111–112*, 562–570.
[52] J. Wang, Y. Ji, G. Jacobs, S. Jones, D. Jung Kim, M. Crocker, *Appl. Catal. B* **2014**, *148–149*, 51–61.
[53] L. Castoldi, R. Bonzi, L. Lietti, P. Forzatti, S. Morandi, G. Ghiotti, S. Dzwigaj, *J. Catal.* **2011**, *282*, 128–144.
[54] Y. Zheng, Y. Liu, M. P. Harold, D. Luss, *Appl. Catal. B* **2014**, *148–149*, 311–321.
[55] D. Mracek, P. Kocia, J.-s. Choi, W. P. Patridge, *Appl. Catal. B* **2016**, *182*, 109–114.
[56] J. Wang, Y. Ji, U. Graham, C. Cesar Spindola de Olivera, M. Crocker, *Chin. J. Catal.* **2011**, *32–5*, 736–745.
[57] N. Ottinger, K. Nguyen, B. Bunting, *SAE Int. J. Fuels Lubr.* **2009**, *2 (1)*, 217–228.
[58] Y. Jia, V. Easterling, U. Graham, C. Fiska, M. Crocker, J.-S. Choi, *Appl. Catal. B* **2011**, *103*, 3–4, 413–427.
[59] V. Easterling, Y. Ji, M. Crocker, J. Ura, J. Theis, R. McCabe, *Catal. Today* **2010**, *151*, 338–346.
[60] J. Wang, Y. Ji, V. Easterling, M. Crocker, M. Dearth, R. McCabe, *Catal. Today* **2011**, *175*, 83–92.
[61] J. Pihl, J. Parks, C. Daw, T. Root, *SAE [Tech. Pap.]* **2006**.
[62] M. Rafigh, R. Dudgeon, J. Pihl, S. Daw, R. Blint, S. Wahiduzzaman, *Emiss. Control Sci. Technol.* **2017**, *3*, 73–92.
[63] H. Schaper, E. Doesburg, L. Van Reijen, *Appl. Catal.* **1983**, *7*, 211–220.
[64] F. Oudet, P. Courtine, A. Vejux, *J. Catal.* **1988**, *114*, 112–120.
[65] J. De Abreu Goes, K. A. T. Wentworth, L. Olsson, *Ind. Eng. Chem. Res.* **2018**, *57*, 9362–9373.
[66] V. Easterling, Y. Ji, M. Crocker, M. Dearth, R. McCabe, *Appl. Catal. B* **2012**, *123–124*, 339–350.
[67] L. Castoldi, R. Matarrese, L. Kubiak, M. Daturi, N. Artioli, S. Pompa, L. Lietti, *Catal. Today* **2019**, *320*, 141–151.
[68] S. Bartova, P. Koci, D. Mracek, M. Marek, J. Pihl, J.-S. Choi, T. Toops, W. Partridge, *Catal. Today*, **2014**, *231*, 145–154.
[69] M. Jablonska, R. Palkovits, *Catal. Sci. Technol.* **2016**, *6*, 7671–7687.
[70] Q. Su, Y. Li, S. Wang, C. Gao, *Top. Catal.* **2013**, *56*, 345–351.
[71] Q. Su, L. Xie, L. Y. X. Qiao, *Can. J. Chem. Eng.* **2014**, *92*, 1579–1586.
[72] H. C. Yao, Y. F. Y. Yao, *J. Catal.* **1984**, *86*, 254–265.
[73] D. Duprez, *J. Chim. Phys.* **1983**, *80*, 487.
[74] F. Dong, T. Tanabe, N. Takahashi, H. Shinjoh, *Catal. Today* **2019**, *332*, 259–266.

Manuscript received: October 28, 2020
Revised manuscript received: December 31, 2020
Version of record online: February 11, 2021